Journal of Alloys and Compounds 914 (2022) 165341

Contents lists available at ScienceDirect

Journal of Alloys and Compounds

journal homepage: www.elsevier.com/locate/jalcom

Characterization of hot deformation behavior of $Al_{0.3}CoCrFeNi$ high-entropy alloy and development of processing map

Madan Patnamsetty[a,*], Sumit Ghosh[b], Mahesh C. Somani[b], Pasi Peura[a]

[a] Materials Science and Environmental Engineering, Tampere University, 33720 Tampere, Finland
[b] Materials and Mechanical Engineering, Centre for Advanced Steels Research, University of Oulu, 90014 Oulu, Finland

ARTICLE INFO

Article history:
Received 1 February 2022
Received in revised form 1 May 2022
Accepted 5 May 2022
Available online 10 May 2022

Keywords:
High Entropy Alloys
Hot deformation
Zener–Holloman Parameter
Dynamic Materials Model
Dynamic recrystallization
Particle stimulated nucleation

ABSTRACT

This study presents the characteristics of hot deformation behavior of a $Al_{0.3}CoCrFeNi$ high–entropy alloy in the temperature and strain rate ranges of 1023–1423 K and 10^{-3}–10 s^{-1}, respectively. The constitutive flow behavior was modeled based on the hyperbolic–sinusoidal Arrhenius–type equations and a mathematical relation was used to observe the influence of true strain on material constants. To define the hot workability of the alloy, a processing map was developed based on the principles of the dynamic materials model. Accordingly, a dynamic recrystallization (DRX) domain was identified as prudent for processing in the temperature and strain rate ranges of 1273–1423 K and 10^{-2}–2×10^{-1} s^{-1} respectively, with a peak efficiency of ~45% at 1423 K/6×10^{-2} s^{-1}. At lower temperatures (1048–1148 K) and strain rates (10^{-3}–3×10^{-3} s^{-1}), a dynamic recovery (DRV) domain was identified with a peak efficiency of 38% at 1123 K/10^{-3} s^{-1}. A large instability regime occurred above 3×10^{-1} s^{-1} with an increased tendency of adiabatic shear bands. It extended to lower strain rates 10^{-2}–10^{-1} s^{-1} at temperatures < 1123 K, manifested by localized shear bands and grain boundary cracking. At low strain rates (5×10^{-3}–10^{-3} s^{-1}) and temperatures (1148–1298 K), particle stimulated nucleation of new DRX grains occurred at B_2 precipitates, though the efficiency of power dissipation dropped sharply to ~9%.

1. Introduction

High-entropy alloys (HEAs) have gained significant attention in the recent decade due to their fascinating properties, especially high mechanical strength, ductility, and thermal stability, besides remarkable resistance to wear and corrosion [1]. HEAs mainly comprise of four or more principal alloying elements alloyed in equiatomic or near-equiatomic concentrations. An initial approach in respect of designing a HEA was to obtain a single-phase solid solution with high mixing configurational entropy [2]. The equiatomic CoCrFeMnNi single phase HEA, also known as the Cantor alloy, is one of the earliest and most researched HEA [1,3]. However, a new design approach was considered later to include multiple phases and/ or intermetallic precipitates to enhance the balance between strength and damage tolerance [1,4]. In this regard, $Al_xCoCrFeNi$ (x = 0–2) HEA system is perceived as a potential engineering material, where the addition of Al can facilitate the formation of a BCC phase from the FCC matrix, as Al is a strong BCC stabilizer. At low Al-level corresponding to x = 0–0.5, the alloy continues to have the FCC structure, but with a further increase in Al content in the range x = 0.5–0.9, both FCC and BCC structures do coexist. However, a significant increase in Al-addition in excess of x = 0.9 facilitates complete stabilization of BCC structure [5,6]. Accordingly, the $Al_xCoCrFeNi$ HEA system has attracted a wide research interest due to its extraordinary physical and mechanical properties [7]. For example, as-cast $Al_{0.3}CoCrFeNi$ HEA showed a nominal tensile strength of ~300 MPa with a high ductility of 60%. However, a combination of severe cold rolling reduction of 90% followed by aging at 823 K boosted the tensile strength to as high as 1850 MPa, though with a low elongation of ~5%, largely due to the precipitation of Al–Ni based B_2 and/ or σ nano–precipitates [8]. In yet another study, to achieve a good strength-ductility combination, a cold–rolled $Al_{0.3}CoCrFeNi$ alloy sample with 70% reduction was aged at 1073 K, which did impart not only a reasonably high tensile strength of ~1060 MPa, but also boosted the tensile ductility to ~26% [9]. The possibility of attaining a significant change in the structure, phase fractions and mechanical properties such as excellent impact toughness [10], wear resistance [11], fatigue resistance [12] and excellent work hardening due to twinning [13] induced as a result of Al addition, rendered the alloy system a desirable candidate for structural applications.

* Corresponding author.
E-mail address: madan.patnamsetty@tuni.fi (M. Patnamsetty).

https://doi.org/10.1016/j.jallcom.2022.165341
0925-8388/

Mechanical processing at high temperatures is inevitably necessary not only in shaping engineering materials to useful components, but also to impart desired microstructures and properties. This is governed by the hot workability of the material, which refers to the ease with which the material can be deformed without the onset of defects or fracture. The intrinsic workability of an alloy is affected by its prior processing history, composition, initial microstructure, and dynamic response to a set of deformation conditions. The material response to the imposed hot deformation conditions can be mathematically expressed in terms of constitutive equations. These equations can be useful in predicting the flow stress values at different strains, strain rates and temperatures within the limits of hot deformation, besides the activation energy of hot deformation (Q_{def}). In addition, various material constants that describe the behavior of material under hot deformation conditions are estimated using the constitutive equations [14].

The studies available in the literature illustrating the influence of hot deformation on the microstructural evolution of $Al_{0.3}$CoCrFeNi HEA are limited. Haghdadi et al. [15] reported the occurrence of dynamic recrystallization (DRX) during the hot deformation of $Al_{0.3}$CoCrFeNi HEA at 5×10^{-3} s^{-1}along the prior grain boundaries followed by twinning. In addition, a micro-shear band induced recrystallization was also observed due to strain localization. However, studies illustrating the constitutive flow behavior are limited. Earlier, Tong et al. [16] reported the hot deformation behavior of as-cast and homogenized $Al_{0.3}$CoCrFeNi HEA, but the temperature range was narrow (1023–1223 K) and the strain rate too was varied in a relatively lower range of 5×10^{-4}–10^{-1} s^{-1}. Also, Zhang et al. [17] and Jeong et al. [18] investigated the hot deformation behavior of as-cast and homogenized $Al_{0.5}$CoCrFeNi and $Al_{0.7}$CoCrFeMnNi alloys, but the temperature ranges of deformation were quite narrow in the ranges 1123–1273 K and 1173–1373 K, respectively, though the strain rate was varied in a wide range of 10^{-3}–10 s^{-1} for both materials. Wang et al. [19] also investigated the influence of hot deformation as well as heat treatment on the resultant microstructures of $Al_{0.3}$CoCrFeNi HEA and reported the occurrence of microstructural refinement through DRX, besides the formation of B_2 precipitates following certain heat treatments. In addition, Gwalani et al. [20] calculated the activation energy of grain growth (~486 kJ/mol) for $Al_{0.3}$CoCrFeNi alloy subjected to heavy cold rolling (~90% reduction) and subsequent aging at different temperatures (1223, 1348 and 1423 K). Annasamy et al. [21], on the other hand, determined the activation energy of static recrystallization (Q_s = ~549 kJ/mol) and estimated a relatively high grain growth exponent (n_s = 5), though the temperature range was quite narrow (1073–1173 K). The high Q_s as well as n_s were attributed to the appreciable pinning effect of B_2 precipitates.

There are several phenomenological constitutive models existing in literature to characterize the flow behavior of alloys, such as Zerilli-Armstrong model [22], the Khan-Huang-Liang model [23] and Johnson-Cook model [24]. However, the model proposed by Sellars and McTegart [25] is the most pronounced model to formulate the hyperbolic sinusoidal Arrhenius (HSA) type equations for high temperature deformation conditions. Tong et al. [25] used the HSA type model to determine the constitutive equation for the $Al_{0.3}$CoCrFeNi HEA at a true strain of 0.7, encompassing low strain rates in the range 5×10^{-4}–10^{-1} s^{-1} and temperatures in a narrow range of 1023–1223 K. However, no attempt was made to establish the constitutive equations for $Al_{0.3}$CoCrFeNi HEA in a broad range of temperatures and strain rates [26], particularly using the iterative strain method [27,28] and is considered to be one of the main research gaps. While trial–and–error methods are generally employed in selecting the hot working parameters, a processing map constructed on the basis of dynamic materials model (DMM) can become an explicit representation of the constitutive behavior of the material enabling optimization of the hot workability, while controlling the microstructure, and excluding the cracking and instability regimes that need to be avoided for defect–free processing [14]. In addition, it is possible to identify a 'safe' hot workability domain comprising ideal deformation conditions. In particular, the domain of dynamic recrystallization (DRX) is important, since this process reconstitutes the microstructure and enhances the hot workability. In literature, there are only few studies on the development of processing maps of HEAs, such as CoCrFeMnNi [29], $Al_{0.5}$CoCrFeMnNi [30], $Al_{0.7}$CoCrFeNi [18] and FeCrCuNi$_2$Mn$_2$ [28], illustrating their hot workability and constitutive models. However, these studies offer only a limited in-depth analysis in terms of the evolution of microstructures without encompassing all the deterministic domains of the processing maps. There are only a few studies available in the literature on the hot workability of HEAs correlating the detailed microstructural features of each domain/regime of the processing map, such as in the cases of CoCrFeMnNi [29], FeCrCuNi$_2$Mn$_2$ [28], $Sn_{0.5}$CoCrFeMnNi [31], $Al_{0.7}$CoCrFeNi [18] and MoNbHfZrTi [32] HEAs, etc.

The current objective is to characterize the hot deformation behavior of a $Al_{0.3}$CoCrFeNi using isothermal compression tests at various constant true strain rates and temperatures in the range 10^{-3}–10 s^{-1} and 1023–1423 K, respectively, conducted on a Gleeble® 3800 thermomechanical simulator. Efforts were directed towards interpreting the influence of processing parameters on the hot deformation behavior and microstructural evolution. The flow stress data were analyzed to develop an iterative method using the hyperbolic sinusoidal Arrhenius type approach to establish constitutive equations in order to be able to accurately predict the flow stress of the alloy as a function of strain, strain rate and temperature. The impact of true strain was incorporated over a wide strain range of 0.2–0.75. Besides, processing maps were constructed based on the principles of DMM in order to optimize the hot workability of the alloy and identify a 'safe' processing domain for defect–free processing of the alloy. Furthermore, different deterministic domains as well as cracking and instability regimes were characterized using various techniques, such as electron backscatter diffraction (EBSD), optical microscopy (OM), and transmission electron microscopy (TEM) to understand the occurrence of respective microstructural mechanisms.

2. Experimental details

The experimental $Al_{0.3}$CoCrFeNi HEA was melted in a vacuum induction melting furnace under inert argon atmosphere with 99.9% pure elemental powders and fabricated into a rectangular ingot of dimensions ~140×40×40 mm and weighing ~2 kg. To ensure complete melting of the elemental powders and to promote homogeneous mixing, the melted alloy was held for ~1 min in the liquid state prior to casting. The casting was homogenized at 1473 K for 24 h in a furnace maintained under argon atmosphere and cooled to room temperature inside the furnace. The homogenized casting was hot rolled at 1323 K to a thickness of 11 mm in 26 passes with a total rolling reduction of ~70%. The alloy was reheated in the furnace for about 10 min after every pass to maintain the rolling temperature at 1323 K for subsequent passes. Specimens from the hot rolled $Al_{0.3}$CoCrFeNi HEA were extracted in the traverse-normal direction using the wire-cut electric discharge machining (EDM) technique. The dimensions of the samples were ϕ 8 mm × 10 mm with an aspect ratio of 1.25.

High temperature compression tests were conducted on the Gleeble thermo-mechanical simulator. The temperature of the specimens was monitored using the thermocouple spot-welded at the

center of the curved surface. The hot compression tests were conducted similarly as done in the authors' previous work [27,29], in the temperature range of 1023–1423 K in steps of 50 K and the strain rate was varied in the range 10^{-3}–10 s^{-1} in steps of one order of magnitude. Initially, the specimens were reheated to 1423 K at a heating rate of 20 K/s and held for 5 min, then cooled to the deformation temperature at a cooling rate of 20 K/s and held for 15 s to allow the temperature to even out prior to hot compression. In order to reduce the friction and minimize barreling effect during hot compression, a graphite foil was used between the parallel surface of the specimen and the anvil on both sides. In order to reduce the temperature gradient and prevent the specimen from sticking to anvils, a tantalum foil was used between the anvil and the graphite foil. After compression tests, the compressed air was used for cooling. The hot compression data was evaluated using the MATLAB® 2020a program and true stress–true strain plots made using the Origin® 2017 software.

The microstructure of the specimens was examined using a Zeiss ULTRAplus field emission scanning electron microscope equipped for both elemental analysis (Oxford Instruments X–Max^N 80 energy dispersive X-ray spectroscope (EDS)) and crystallographic analysis (Oxford Instruments' Symmetry® electron backscatter diffraction (EBSD) detector). The hot deformed specimens were segmented along the mid-plane parallel to the compression axis, as also explained in author's previous work [33]. The samples were first rough-polished using successive abrasive SiC papers, and in the final stages, fine-polished with 3 and 1 µm diamond suspensions. Finally, a 0.04 µm silica colloidal suspension was used in the final step of polishing. The working voltage for FESEM was 20 kV and the step size for EBSD data acquisition was 0.7 µm. The EBSD measurements made on select specimens were further processed using the CHANNEL 5 data package. The grain boundaries (GBs) were categorized as low angle grain boundaries (LAGBs) with misorientation angle (φ) in the range of $2° < \varphi < 15°$ and high angle grain boundaries (HAGBs) with misorientation angle (φ) ≥ 15°, in order to determine the characteristics of microstructural evolution. HAGBs were delineated to determine the grain sizes. Besides, the $\Sigma 3$ twin (CSL) boundary regions with misorientation angle (φ) of 60 ± 5° were excepted from the grain size evaluation. Furthermore, the fully recrystallized, partially deformed, and deformed grains were identified using the grain average misorientation (GAM) maps. The GAM maps were constructed using the EBSD data according to the criteria explained in previous work [33]. A PANalytic Empyrean Multipurpose Diffractometer (Malvern Panalytical Ltd, Netherlands) X-ray diffraction (XRD) instrument was used to examine the crystallographic structure of the hot-rolled sample, operated on a Cu-K_α radiation source at 45 kV and 40 mA conditions. The respective XRD data in 2θ range was collected between 30° and 110° with a step size of 0.013°. A JEOL 2200FS EFTEM/STEM operated at 200 kV was used to conduct the transmission electron microscopy (TEM) study on select specimens, enabling resolution at high magnification to resolve the evolution and co-existence of secondary phases/precipitates and to illustrate detailed structural changes by indexing concerned selected area electron diffraction (SAED) patterns. Variations in composition of different phases were analyzed using the energy dispersive spectroscopy (EDS) in STEM mode. Focused ion beam (FIB) technique was used to section thin lamellas from the specimens for the TEM analysis.

3. Results and discussion

3.1. Initial microstructure

The chemical composition of the hot rolled $Al_{0.3}$CoCrFeNi HEA was estimated by taking an average of three EDS measurements made in different locations of the sample, Table 1. The initial microstructure in hot rolled condition prior to isothermal compression testing was examined using OM and EBSD imaging. The representative OM and EBSD inverse pole figure (IPF) map are shown in Fig. 1a and b, respectively, revealing the equiaxed grain structure. The average grain size based on the EBSD maps was estimated to be ~52 µm. In addition, the XRD pattern illustrating characteristic diffracted peaks corresponding to different crystallographic planes indicate that the FCC is the most stable phase throughout the microstructure.

3.2. Flow stress behavior

Fig. 2a–i show typical true stress–strain curves of the $Al_{0.3}$CoCrFeNi plotted from the hot compression data in the temperature and strain rate ranges of 1023–1423 K and 10^{-3}–10 s^{-1}, respectively. The figure clearly depicts the change in flow stress behavior with respect to strain rate and/or deformation temperature. Irrespective of the strain rate, at initial strains up to ~0.3 true strain, the flow stress increased with increasing true strain in all the test conditions obviously due to work hardening, which is due to the proliferation and movement of dislocations at initial strains. In general, the work hardening rate and peak stress expectedly increased with a decrease in temperature and an increase in strain rate, i.e., with increasing Zener-Hollomon parameter (Z).

A characteristic peak stress behavior is seen in flow curves at all test temperatures and low strain rates (10^{-2} and 10^{-1} s^{-1}), followed by flow softening on further straining. This is a typical behavior of DRX that is observed during the high temperature compression of FCC based alloys with low or intermediate stacking fault energies (SFE) [27]. At higher temperatures (1323–1423 K) and lower strain rates (10^{-2}–10^{-3} s^{-1}), a typical peak stress and flow softening behavior followed by steady-state was achieved in the flow stress curves, suggesting that the DRX process was complete, and the grain growth occurred. Similarly, at 10^{-3} s^{-1} and temperatures 1023–1073 K, features typical of softening due to flow localization were observed. However, with further increase in temperature (1123–1273 K) at 10^{-3} s^{-1}, the flow softening gradually disappeared with flow stress behavior becoming nearly steady–state, typical of dynamic recovery (DRV).

At high strain rates (1 and 10 s^{-1}) and at all temperatures ≤ 1123 K, typical strain hardening behavior is evident as the flow stress increases with strain, whereas at temperatures in the range of 1173–1223 K, the flow softening is observed, though without any specific trend and at times approaching steady-state, which is reminiscent of a dynamic balance between strain hardening and flow softening due to dynamic recovery. Further, at high temperatures (1273–1423 K), the flow stress behavior generally remained as steady-state with increasing strain and temperature, without showing any evidence of flow softening (Fig. 2f–i) unlike seen at lower temperatures (≤1123 K) at the same strain rates.

Table 1
Chemical composition of hot rolled $Al_{0.3}$CoCrFeNi based on EDS analysis.

Elements	Al	Co	Cr	Fe	Ni
at%	6.98 ± 0.2	23.25 ± 0.1	23.89 ± 0.1	23.25 ± 0.1	22.60 ± 0.4

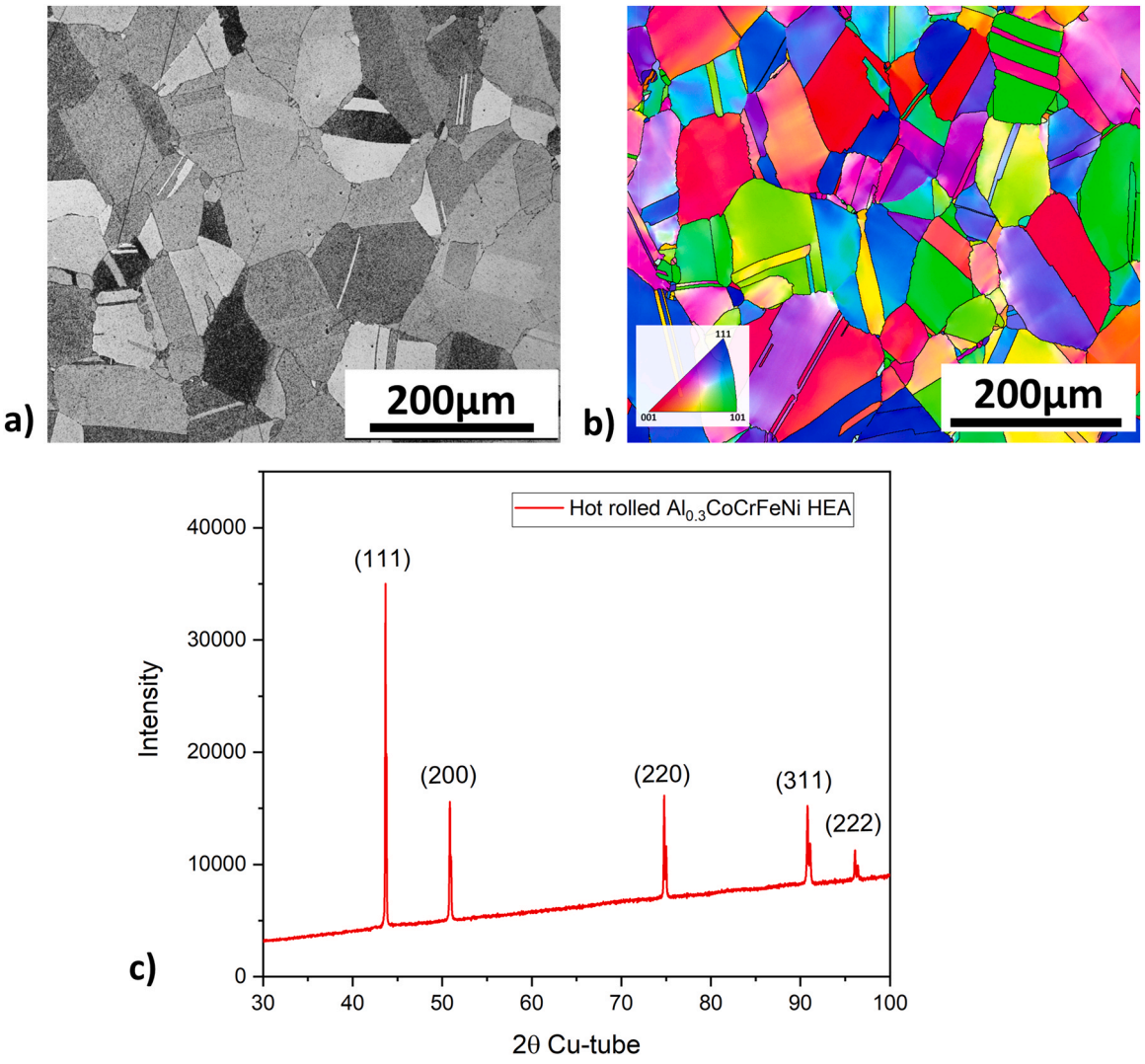

Fig. 1. a) Optical micrograph; b) EBSD IPF map; c) XRD pattern of the hot rolled $Al_{0.3}$CoCrFeNi.

3.3. Arrhenius type constitutive equation

The constitutive equation based on hyperbolic sinusoidal Arrhenius (HSA) type model that describes the flow stress of $Al_{0.3}$CoCrFeNi at $\varepsilon = 0.6$, as explained in the supplementary section, can be expressed as follows:

$$\sigma_{0.6} = \frac{1}{0.0046}\cdot ln\left\{\left(\frac{Z_{0.6}}{7\cdot 10^{11}}\right)^{\frac{1}{4.32}} + \left[\left(\frac{Z_{0.6}}{7\cdot 10^{11}}\right)^{\frac{2}{4.32}} + 1\right]^{1/2}\right\} \quad (1)$$

where the Z at $\varepsilon = 0.6$ is expressed as:

$$Z_{0.6} = \dot{\varepsilon}\cdot\exp\left(\frac{308300}{RT}\right) \quad (2)$$

Additionally, by substituting the material constants α, n, A and Q_{def} in Eq. S5 (in Supplementary section), the constitutive relationship between $\dot{\varepsilon}$, T and σ at $\varepsilon = 0.6$ can be expressed as:

$$\dot{\varepsilon} = 7\cdot 10^{11}\cdot[\sinh(0.0046\cdot\sigma_{0.6})]^{4.32}\cdot\exp\ (-308300/RT) \quad (3)$$

In order to define the flow stress behavior of $Al_{0.3}$CoCrFeNi HEA at different strains over a wide strain range, the material constants α, n, Q_{def}, and A need to be calculated through regression analysis considering the flow stress data at different ε values in the range 0.2–0.75, at a step size of 0.05 strain. The relationships between the strains and material constants were fitted using sixth–order polynomials (Fig. 3). Thus, the regression equations of the respective material constants α, n and A, and Q_{def} in the range 1023–1423 K as a function of strain can be reasonably described by Eqs. (4)–(7), respectively, as given below:

$$\alpha = 0.0108 - 0.0816\cdot\varepsilon + 0.4045\cdot\varepsilon^2 - 1.055\cdot\varepsilon^3 + 1.551\cdot\varepsilon^4 - 1.2088\cdot\varepsilon^5 + 0.3884\cdot\varepsilon^6 \quad (4)$$

$$n = 21.375 - 102.94\cdot\varepsilon + 280.2\cdot\varepsilon^2 - 460.17\cdot\varepsilon^3 + 500.52\cdot\varepsilon^4 - 346.25\cdot\varepsilon^5 + 113.51\cdot\varepsilon^6 \quad (5)$$

$$Q_{def} = 303.37 + 2359.7\cdot\varepsilon - 15375\cdot\varepsilon^2 + 40513\cdot\varepsilon^3 - 52976\cdot\varepsilon^4 + 33587\cdot\varepsilon^5 - 7996.5\cdot\varepsilon^6 \quad (6)$$

$$lnA = 21.351 + 333.06\cdot\varepsilon - 2089.3\cdot\varepsilon^2 + 5564.5\cdot\varepsilon^3 - 7511.9\cdot\varepsilon^4 + 5026.2\cdot\varepsilon^5 - 1308\cdot\varepsilon^6 \quad (7)$$

3.3.1. Material parameters

At 0.6 true strain, the $\left[\frac{\partial ln\dot{\varepsilon}}{\partial ln\,[\sinh(\alpha\sigma)]}\right]_T$ values varied between 5.75 and 4.03 with the temperature varying in the range 1023–1423 K, and the corresponding mean value of n was estimated to be 4.32. The value of n is generally greater than 5 in the case of dislocation – precipitate interaction [16]. For example, a study by Gwalani et al. [8]

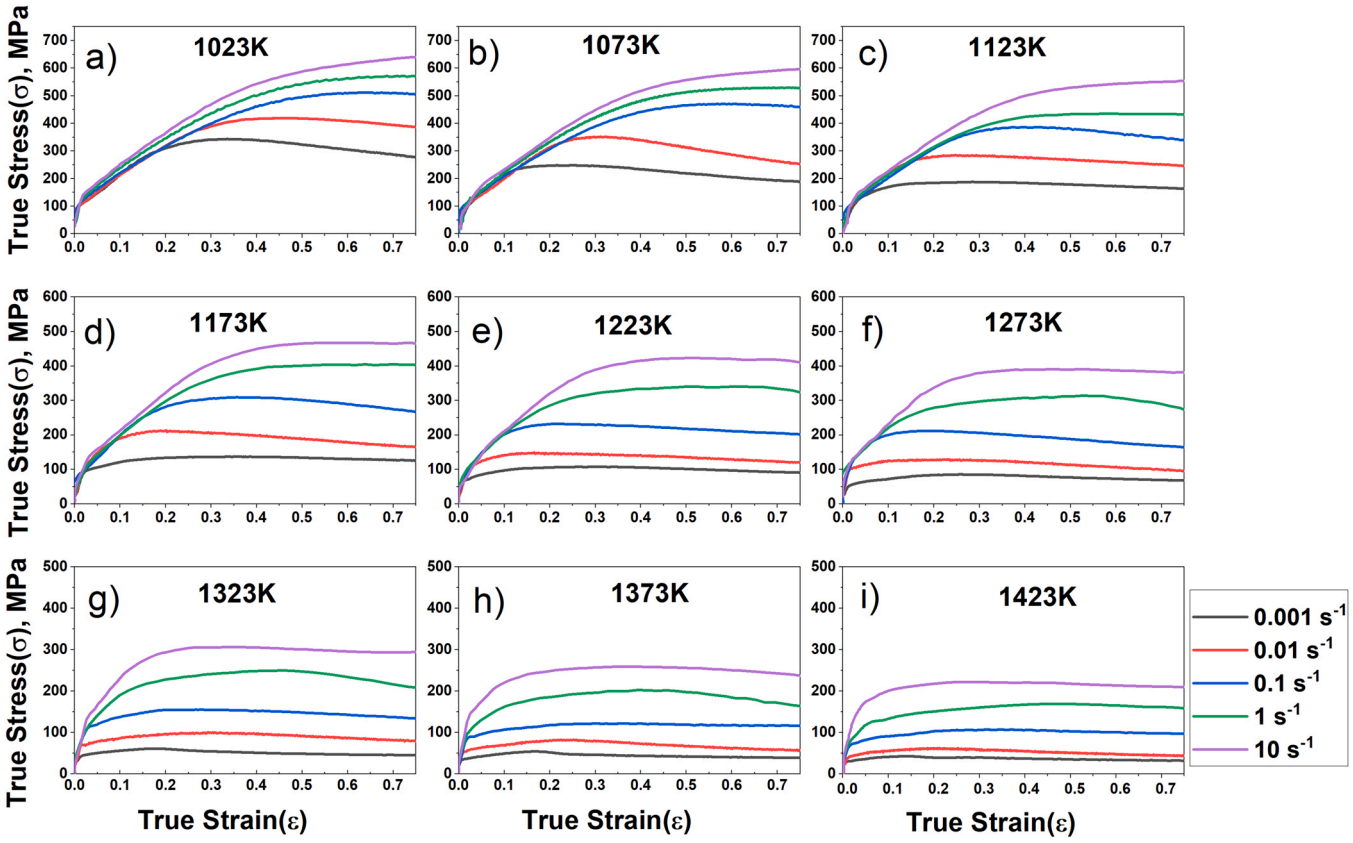

Fig. 2. True stress – true strain curves different temperatures and strain rates.

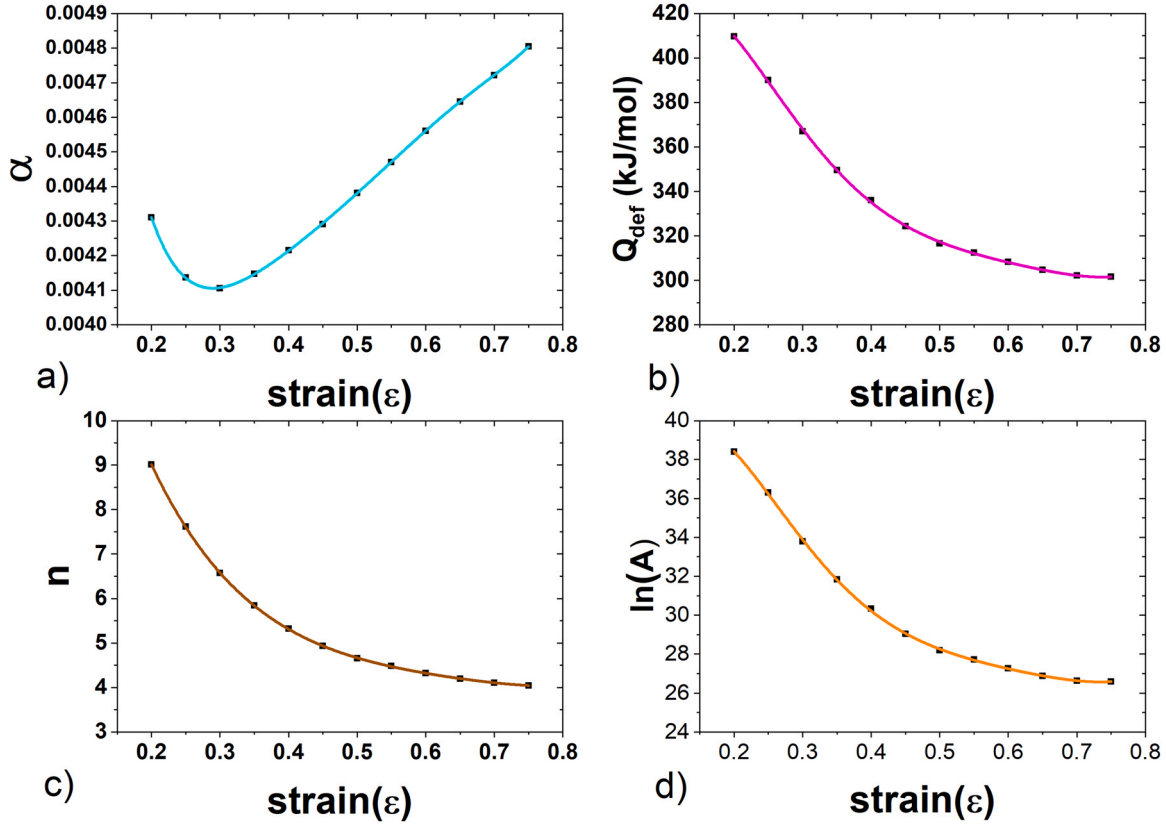

Fig. 3. Variation of model parameters with strain: (a) α vs ε (b) Q_{def} vs ε (c) n vs ε and (d) lnA vs ε.

has shown that B_2 precipitate formed above 823 K. According to their CALPHAD predictions, B_2 precipitate is thermodynamically stable up to 1373 K, though its stability decreases with the increase in temperature. In addition, a study by Tong et al. [16] on hot deformation behavior of $Al_{0.3}$CoCrFeNi HEA has reported that the hot deformation at temperatures below 1223 K resulted in dynamic precipitation of B_2 precipitates along the grain boundaries that interacted with the dislocations. Eventually, the passage of dislocations led to the formation of Orowan dislocation loops around the B_2 precipitates during hot deformation. Therefore, the resistance to dislocation motion increased with n approaching a value greater than 5. However, it should be noted that Tong et al. [16] reported the n value to be 4.87 at 0.7 strain. The lower n value in their study [16] might be due to the narrow test temperature range of 1023–1223 K with the strain rates in the range 5×10^{-4}–10^{-1} s^{-1}. The existence of B_2 precipitates along the GBs was also confirmed in the current $Al_{0.3}$CoCrFeNi alloy at 1123 K/10^{-3} s^{-1}, identified by SEM investigations combined with EDS mapping, and the concerned results will be presented later in Section 3.4.2. Apparently, the formation of these precipitates must have influenced the hot deformation characteristics and eventually increased the n–value. On the other hand, an increase in temperature would decrease the thermodynamic stability of B_2 precipitates, which *might* decrease the value of n. As depicted in Fig. 3c, the variation of n has been expressed as a function of true strain in the range 0.2–0.75 (Eq. (5)). In the current study, the n–value varied in the range 9.01 – 4.04. This shows that at low true strains, n–value at all temperatures stays high due to the combined effect of work hardening and resistance to dislocation motion *caused by* B_2 precipitates. Further increase in strain reduced the value of n due to the onset of flow softening and/or steady-state behavior in other test conditions.

Additionally, the material constant α, varied in the range 0.0043–0.0048 (Fig. 3a), and the corresponding value at a true strain of 0.6 was 0.0046. In comparison, Tong et al. [16] reported a value of 0.0038 at 0.7 true strain. However, their hot deformation experiments were limited to a narrow temperature range of 1023–1223 K with *the* strain rate varying in the lower range of 5×10^{-4}–10^{-1} s^{-1}.

Similarly, Q_{def} was calculated at true strains in the range 0.2–0.75 using Eq. (6). For example, at $\varepsilon = 0.6$, the calculated Q_{def} value is ~308 kJ/mol. In the current research work, the estimated Q_{def} varied with strain in the range ~410–302 kJ/mol, as shown in Fig. 3b. This is because the dislocation generation is high at initial strains, and the motion of dislocations is restricted due to the formation of B_2 precipitates. Therefore, the Q_{def} stayed initially high, and further straining led to either flow softening or steady-state behavior in most of the test conditions, thereby reducing the Q_{def} with an increase in strain. In comparison [16], hot deformation at low test temperatures and strain rates resulted in Q_{def} = 394 kJ/mol at 0.7 true strain.

3.3.2. Validation of the hyperbolic–sinusoidal Arrhenius–type model

In order to check the reliability of the hyperbolic sinusoidal Arrhenius type model, the predicted flow stress data over broad ranges of temperatures, strains and strain rates are presented in Fig. 4. The predicted flow stress values are based on Eq. S8 (see Supplementary section) and Eqs. (4)–(7) for all strains in the range 0.2–0.75. Fig. (4) shows that the agreement between the predicted and experimental flow stress data is satisfactory for most of the tests. However, the average fit of the material constants shows significant deviations in flow stress data at high strain rates (1–10 s^{-1}) and low temperatures (1023–1123 K). This is because Eq. S3 and S4 (in the supplementary section) apply to low and high stress levels, respectively and the approach used is to obtain the values of n′ and β using the respective equations. Therefore, these small deviations can occur depending on the accuracy of the least squares fits and differences in the slopes at different temperatures [34]. Such deviations ultimately affect the values of material constants.

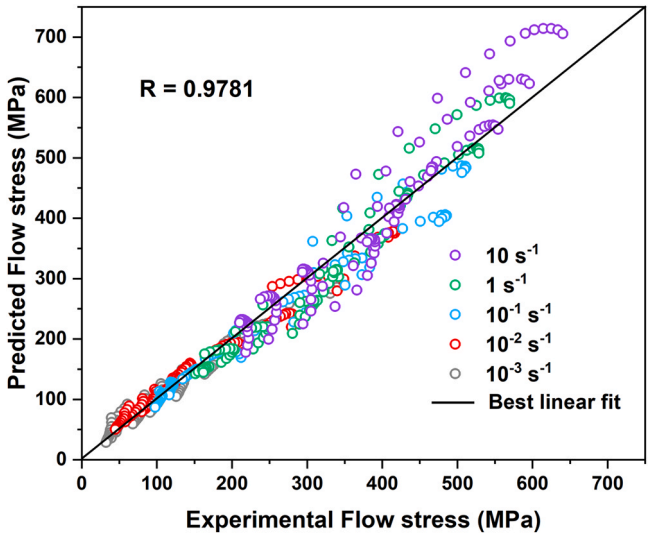

Fig. 4. Comparison of Predicted vs. experimental flow–stress data of $Al_{0.3}$CoCrFeNi HEA.

To assess the degree of difference between the predicted and experimental values, a standard statistical method such as the correlation coefficient (R) and the average absolute relative error (AARE), are used as detailed in previous work [27]. The cumulative AARE was 9.66%, suggesting a reasonably good fit to the experimental data. The R for the least squares fit through the experimental data is 0.9781, revealing a good relationship between predicted flow stress and experimental data. Fig. 5 shows the predicted flow stress curves (dashed lines) plotted in comparison with the experimental true stress–true strain curves (full lines). The deviations in flow stress behaviors were significant at high strain rates, particularly at 10 s^{-1} in the low temperature regime of 1023–1123 K.

3.4. Processing maps

The approach to the construction of 2D iso–efficiency contour maps and instability maps based on the concepts of DMM is precisely explained in the Supplementary section. In order to demarcate various deterministic domains and low efficiency and instability regimes, a processing map was constructed by superimposing the respective 2D instability contour plots (Fig. S3d) on the 2D iso-efficiency contour map (Fig. S3b) at different strains (ε = 0.4, 0.5 and 0.6), as shown in Fig. 6a–c, respectively. The three processing maps shown in Fig. 6a–c, have a close correspondence. It is obvious that all the domains/regimes of the processing maps at different strains show almost similar characteristics. In all, two deterministic domains and two low efficiency regimes with closely spaced iso-–efficiency contours were identified in the processing map regardless of the strain (Fig. 6). Consequently, a conceptual processing map was constructed at $\varepsilon = 0.6$ marking all the domains and regimes as shown in Fig. 7a. The increase in strain varied the peak/ trough efficiencies of the two domains (B, C) and two regimes (D, E) as shown in Fig. 7b. The region marked as A is the instability regime. The domains with peak efficiencies, and regimes with low efficiencies (Fig. 7a and b) are listed as below.

1. A domain (Region B) with a peak at ~1423 K/6×10^{-2} s^{-1} has a high efficiency in the range of ~37–46%, increasing slightly with increase in strain.

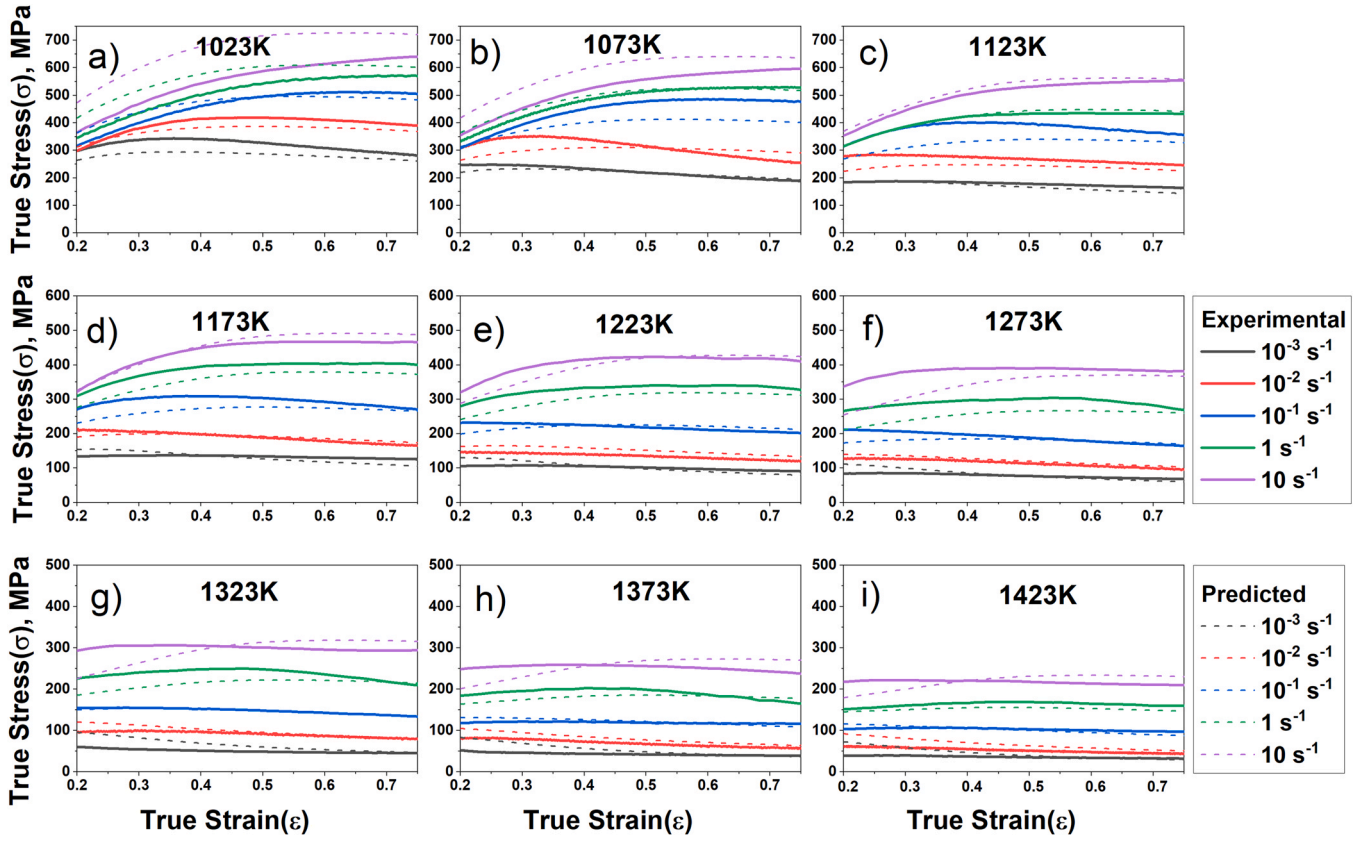

Fig. 5. Predicted flow stress curves based on hyperbolic–sinusoidal Arrhenius type model vs. experimental true stress–strain curves at different temperatures and strain rates.

2. A domain (Region C) with the peak at 1123 K/10^{-3} s^{-1} has a high efficiency varying from ~41% at 0.2 ε to ~36% at 0.7ε, first increasing and then decreasing mildly with increase in strain.
3. A regime (Region D) at 1223 K/10^{-3} s^{-1} has a low efficiency decreasing from ~23–9% with increase in ε from 0.2 to 0.7.
4. A regime (Region E) at 1423 K/10^{-3} s^{-1} has a low efficiency varying in a narrow range from ~21% at 0.2 ε to 12% at 0.7ε.

3.4.1. Region B (Domain at 1423 K/6 ×10^{-2} s^{-1})

This domain extends over the temperature and strain rate ranges of 1273–1423 K and 10^{-2}– 2 × 10^{-1} s^{-1}, respectively. In this domain, a minor increment in the peak efficiency from 37% to 46% is observed, as shown Fig. 7b, which is relatively uniform with an increase in strain. In addition, it is observed that the flow stress decreased with an increase in strain following the peak stress behavior in the true stress – strain curves (Fig. 2f–i), which is quite typical for DRX in low SFE materials. The current $Al_{0.3}$CoCrFeNi HEA is also reported as a low SFE material [35–37]. The fine DRX grains distributed along prior elongated GBs in the IQ maps as shown in Fig. 8a–f, suggest that the deformation mechanism is essentially DRX. However, at 1373 and 1423 K/10^{-2} s^{-1}, the prior pancaked grains are almost non-existent and the microstructural reconstitution through the nucleation and growth of DRX grains is apparent. Further, the TEM bright field image of the hot deformed specimen at 1323 K/10^{-2} s^{-1} (Fig. 9a) depicts the co-existence of an equiaxed grain structure with low dislocation density suggesting the formation of DRX grains. B_2 precipitates were not observed in TEM analysis and, only the FCC phase was detected in the DRX domain, based on the SAED pattern recorded on the [110]γ zone axis (Fig. 9b).

Furthermore, the corresponding IQ maps superimposed over GB maps of the specimens deformed in the DRX domain are determined (Fig. 8). The Σ3 twin boundaries are formed along the elongated prior GBs within the DRX grains. The formation of abundant twins within the recrystallized grains is a characteristic of discontinuous DRX in low to medium SFE materials [38]. In addition, the presence of Σ3 twin boundaries within the recrystallized grains was also identified in TEM bright field image of another location of the specimen at 1323 K/10^{-2} s^{-1}, as shown in Fig. 9c. A SAED pattern recorded from the selected location as marked in Fig. 9c clearly shows reciprocal lattice reflection from the Σ3 twin spots in addition to the primary FCC reflections from [011]γ (Fig. 9d).

The rise in temperature resulted in an increase in DRX grain size, Σ3 twin boundaries, and area fractions of DRX grains (f_{DRX}), as shown in Table 2, but the corresponding values decreased with the increase in the strain rate. At a lower strain rate of 10^{-2} s^{-1}, the peak stress was reached at relatively low strain resulting in an early onset of DRX and hence, resulting in increased DRX grain size, Σ3 twin boundaries and f_{DRX}. On the contrary, at 1423 K/10^{-1} s^{-1}, there is a minor decrease in average DRX grain size, Σ3 twin boundary fraction, and f_{DRX}, compared to that at 1373 K/10^{-1} s^{-1}. This is presumably due to somewhat accelerated nucleation and growth of new DRX grains at 1423 K/10^{-1} s^{-1} (Fig. 9d). A minor increase in the fraction of LAGBs in the specimen tested at 1423 K/10^{-1} s^{-1} further confirms the increased instances of DRX at relatively high temperatures. Additionally, the fraction of recrystallized area (blue colored region in GAM map in Fig. 10) increased with an increase in temperature and strain rate.

In earlier studies [15] the evolution of DRX along the prior grain boundaries, was observed due to the hot deformation of FCC $Al_{0.3}$CoCrFeNi at 1303 K/5 × 10^{-3} s^{-1}. In addition, Patnamsetty et al. [29] and Ghosh et al. [33] noticed the existence of Σ3 twin boundaries within DRX grains in the low SFE CoCrFeMnNi during hot deformation in DRX domain covering the temperature and strain rate ranges of 1223–1323 K and 10^{-2}–5 × 10^{-1} s^{-1}, respectively.

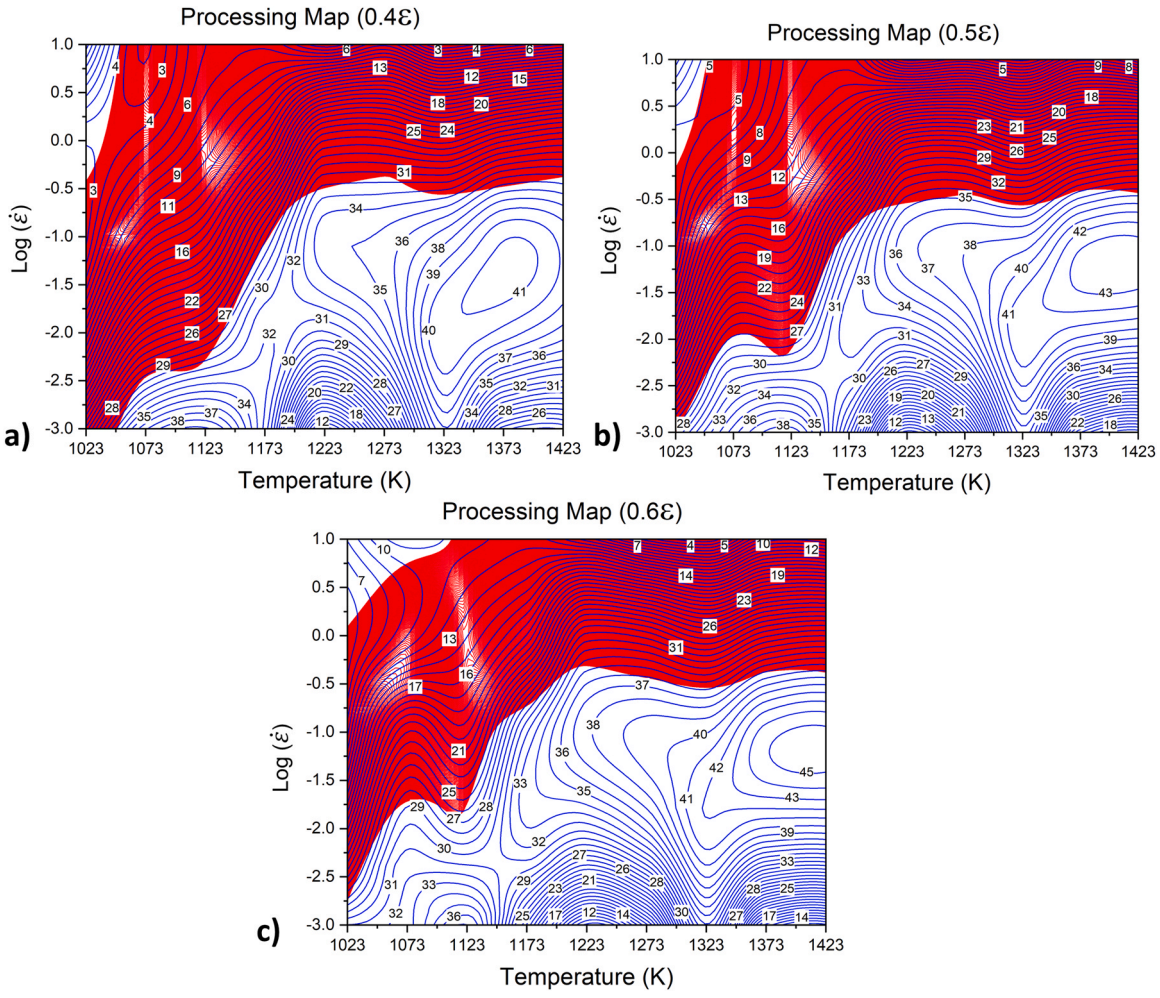

Fig. 6. Processing maps of $Al_{0.3}$CoCrFeNi HEA at different strains: (a) ε = 0.4, (b) ε = 0.5 and (c) ε = 0.6. The region marked as red represents the instability regime.

3.4.2. Region C (Domain at 1123 K/$10^{-3}s^{-1}$)

This domain extends over a strain rate range of 3×10^{-3}–10^{-3} s^{-1} and a temperature range of 1073–1148 K. The representative optical micrographs of the specimens isothermally compressed at 1073 and 1123 K at the strain rate of 10^{-3} s^{-1}, i.e., in the vicinity of the peak efficiency location, are presented in Fig. S4a and b, respectively. Both the micrographs show the presence of elongated grains structures and hence the domain can be broadly called as DRV domain. However, a close examination showed traces of very fine grains along the GBs in some locations, presumably as a consequence of inefficient DRX or even static recrystallization (SRX), marked with arrows in the inset of the EBSD IQ map of the hot deformed specimen at 1123 K/10^{-3} s^{-1} (Fig. 11a). The presence of Σ3 twin boundaries (red colored) within fine grains is also visible in the inset of Fig. 11a. However,

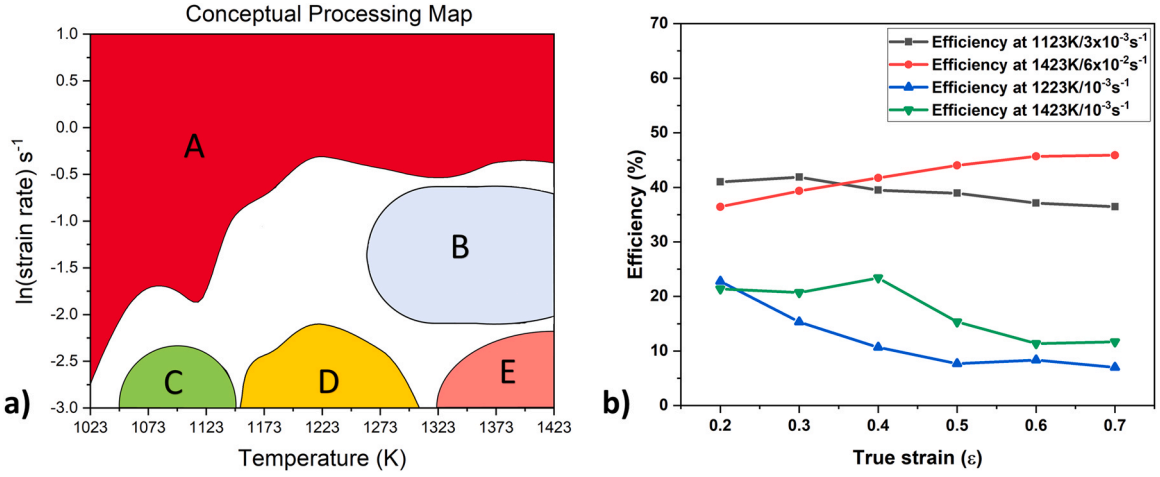

Fig. 7. a) A conceptual processing map marking various domains (B, C), low efficiency regimes (D, E) and instability regime (A). b) Variation of the efficiency of power dissipation (η) with strain for the domains (B, C) and low efficiency regimes (C, E) in the processing map.

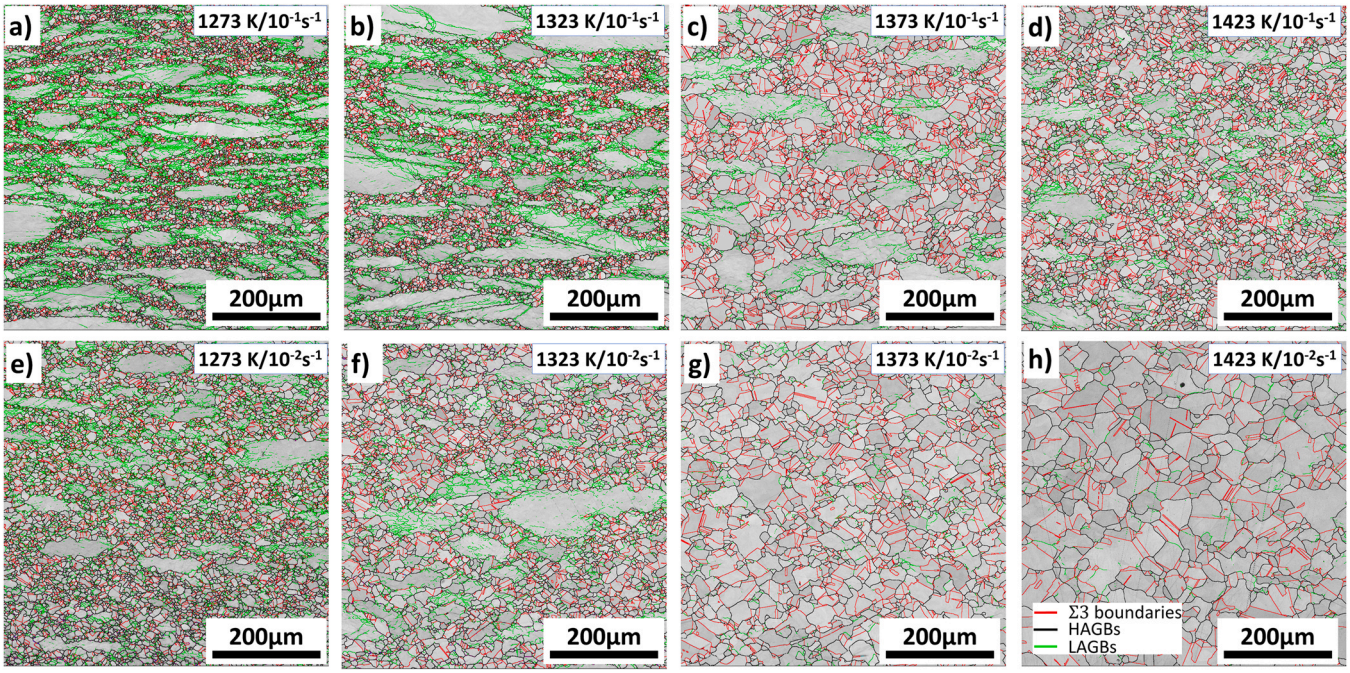

Fig. 8. Image quality (IQ) maps of $Al_{0.3}CoCrFeNi$ HEA deformed at (a)1273 K/10^{-1} s^{-1}; (b) 1323 K/$10^{-1}s^{-1}$; (c)1373 K/$10^{-1}s^{-1}$; (d) 1423 K/10^{-1} s^{-1}; (e)1273 K/10^{-2} s^{-1}; (f) 1323 K/10^{-2} s^{-1}; (g)1373 K/10^{-2} s^{-1}; (h) 1423 K/10^{-2} s^{-1}.

there is no substructure noted in the fine grains. In addition, the GAM map shows the traces of recrystallized grains, marked by blue color in some areas, though its mechanism of formation is not clear (Fig. 11c).

Additionally, from the inset of EBSD phase fraction map (Fig. 11b), the red colored dots, as indicated by an arrow, point to the presence of small formations of B_2 precipitates (BCC) along the prior GBs adjacent to the fine grains. However, fine precipitates (< 80 nm), if any, cannot be resolved by EBSD due to its limit of resolution. At high magnification, SEM back scattered electron (BSE) image (Fig. S5) clearly revealed the existence of precipitates along the grain boundaries. The corresponding EDS maps showed an enrichment of Al and Ni in these precipitates (see Table S1), suggesting the possible dynamic precipitation of B_2, which might have stimulated dynamic or static recrystallization, as it is well known that low SFE materials undergoing hot deformation often display discontinuous DRX [39]. Besides GBs, even subgrain boundaries, second phase particles, and/or shear/deformation bands act as possible nucleation sites for the onset of DRX [39]. It is possible that the particle stimulated nucleation (PSN) at Al–Ni rich B_2 precipitates led to the occurrence of fine grains at the GBs, as is evident in the case of the hot deformed sample at 1123 K/10^{-3} s^{-1} (Fig. 11a, b). However, it is difficult to presume the occurrence of DRX in the absence of substructures, and there is a strong dependence of the occurrence of DRX on strain rate, which is relatively high for low SFE materials. All the same, it is possible that following dynamic precipitation, limited static recrystallization occurred at the B_2 precipitates during subsequent cooling; the stored energy being the driving force for limited SRX. During hot deformation, PSN gives rise to a high local lattice misorientation around the precipitates. These B_2 precipitates can act as potent nucleation sites for new recrystallized grains; with nucleation at a pre-existing subgrain boundary and growth through rapid sub-boundary migration as the main mechanisms during PSN [39].

Under similar test conditions Tong et al. [16] had detected B_2 precipitates and Orowan dislocation looping around the B_2 precipitates. Normally, the GB cracks can occur at low strain rates and low temperatures [14]. But in this case, B_2 precipitates restricted the motion of dislocations by Orowan mechanism, that eventually restricted the pile-up of dislocation along the GBs. In general, the domain can be considered as a dynamic Recovery domain with η varying in a narrow range ~41–36% as a function of strain, though the domain is marked by limited formation of fine grains at the GBs in some locations, which needs further investigation.

3.4.3. Region D (Low efficiency regime at 1223 K/10^{-3} s^{-1})

This regime extends over a temperature range of 1148–1298 K occurring at a relatively low strain rate in the range 5×10^{-3}–10^{-3} s^{-1}. The regime exhibits a low η value dropping sharply with strain from ~23% at 0.2 strain to ~9% at 0.6 strain, and thus, the mechanism in this regime needs to be established. The low and high magnified micrographs of the specimens at 1223 K/10^{-3} s^{-1} (Fig. S6 a, b) show fine and equiaxed grains along the elongated GBs (necklace-type structure) that often contain substructures. Apparently, it seems that there is a possible occurrence of DRX in this regime, though this region is actually a trough with continuously decreasing η value towards the center of the trough. As in the case of DRV domain at 1123 K/10^{-3} s^{-1}, the presence of substructures within the elongated grains and existence of second phase particles noticed along the grain boundaries can be seen in the current regime, as shown in SEM micrographs (Fig. S6c, d). The presence of fine DRX grains together with $\Sigma 3$ twin boundaries (red colored) is clearly visible along the prior/elongated GBs, as presented in the EBSD IQ map (Fig. 12a). In addition, the GAM map further exhibited the recrystallized grains (blue colored region), as shown in Fig. 12c. Presence of B_2 precipitates adjacent to the recrystallized grains was detected through EBSD phase map as well (Fig. 12b).

The existence of dislocation substructures was observed in STEM image, as shown in Fig. S7a along with the presence of fine precipitates. The EDS maps (Fig. S7b–f) clearly revealed that the precipitates were enriched with Ni and Al confirming the formation of

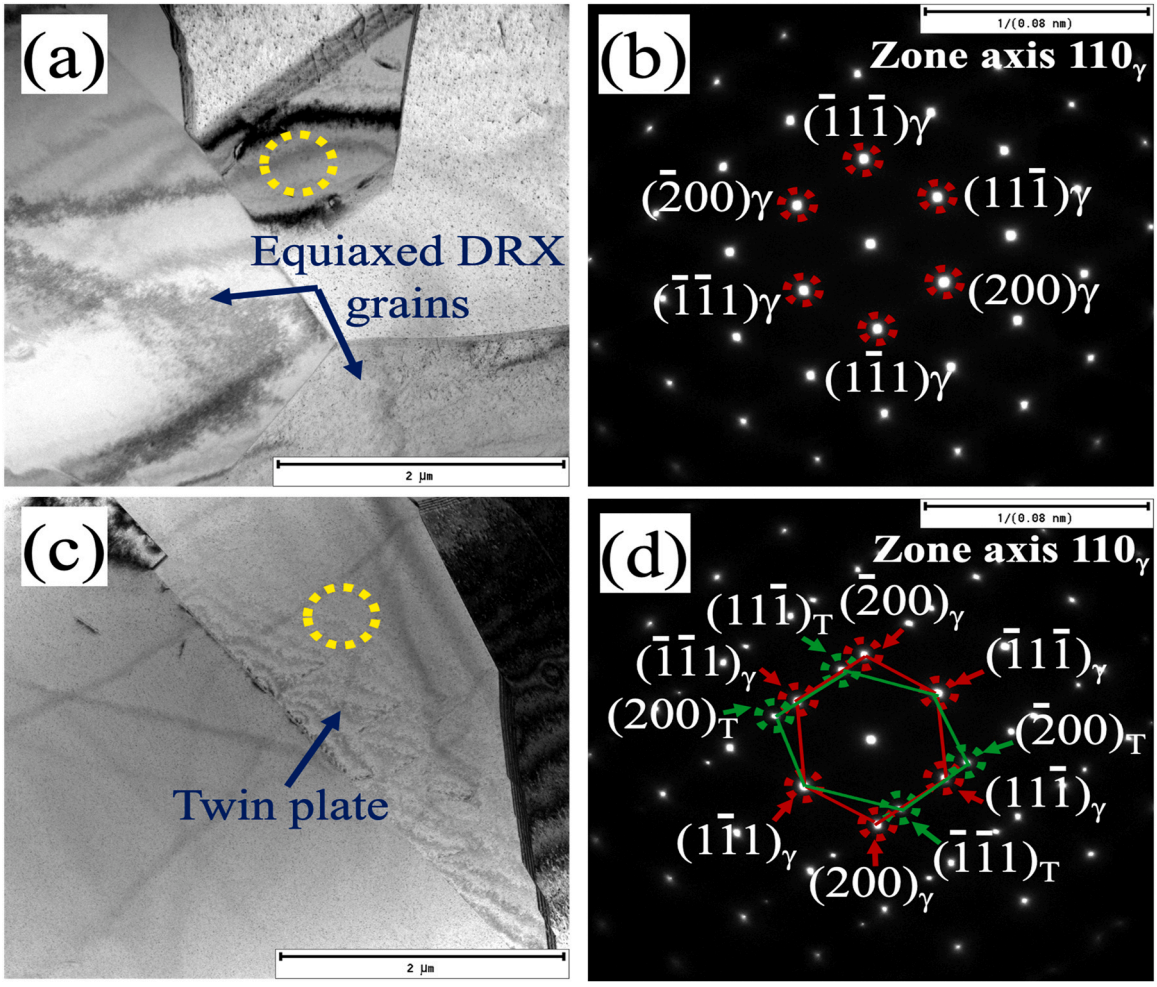

Fig. 9(a) TEM bright field image at 1323 K/10^{-2} s^{-1}, (b) the SAED pattern recorded from the selected location as encircled by yellow color in Fig. 9a along the $[011]_\gamma$ zone axis, (c) TEM bright field image from the selected location at 1323 K/$^{1}0^{-2}$ s^{-1}, contained twins, (d) SAED pattern recorded from the selected location as encircled by yellow color in Fig. 9 c.

B_2 precipitates [16]. Further, the high magnification TEM bright field images of the precipitates are shown in Fig. 13a and c. The corresponding SAED patterns (Fig. 13b and d), were recorded on the $[\bar{1}11]$ and [001] zone axes of the precipitates marked by circles in Fig. 13a and c, respectively, revealing BCC crystal structures. According to TEM observation, it can be further confirmed that these precipitates correspond to B_2 type. Moreover, recrystallized grains were noticed in the vicinity of the precipitates with the presence of dislocation cells around them, as shown in Fig. S7a. During deformation, the possibility of cross slip of dislocations may be effectively hindered by these precipitates, leading to the formation of subgrains. B_2 precipitates formed during deformation at low strain rates (1223 K/10^{-3} s^{-1}), further provide heterogeneous sites for PSN and limited growth of DRX grains, as described in previous Section 3.4.2.

It is surprising that the regime does not show occurrence of any defects or cracks, even though the efficiency of power dissipation remained low and continued to drop sharply as closely spaced iso-efficiency contours. It is tentatively presumed that the main microstructural mechanism in this regime is the occurrence of dynamic precipitation during hot deformation, which is probably a mechanism with the low efficiency of power dissipation. The efficiency drops further with the growth of the precipitates or inefficient PSN of DRX grains at these precipitates, with the growth restricted due to the presence of precipitates, and continued deformation making the

Table 2
DRX grain size, area fraction of recrystallized grains in the DRX domain, different grain boundary fractions and Σ3 twin boundary fractions.

Strain rate	Temperature (K)	D_{DRX} (μm)	f_{DRX} (%)	LAGBs (%)	HAGBs (%)	Σ3 Twin boundaries (%)
10^{-1}	1273	5.36	26.80	60.82	39.18	7.56
	1323	6.78	27.90	59.65	40.35	10.30
	1373	16.02	61.00	34.98	65.02	29.90
	1423	12.36	55.40	37.27	62.73	23.00
10^{-2}	1273	6.13	20.70	59.51	40.49	9.58
	1323	10.96	40.40	45.99	54.01	18.00
	1373	19.93	57.80	24.01	75.99	32.60
	1423	30.41	66.40	26.22	73.78	33.80

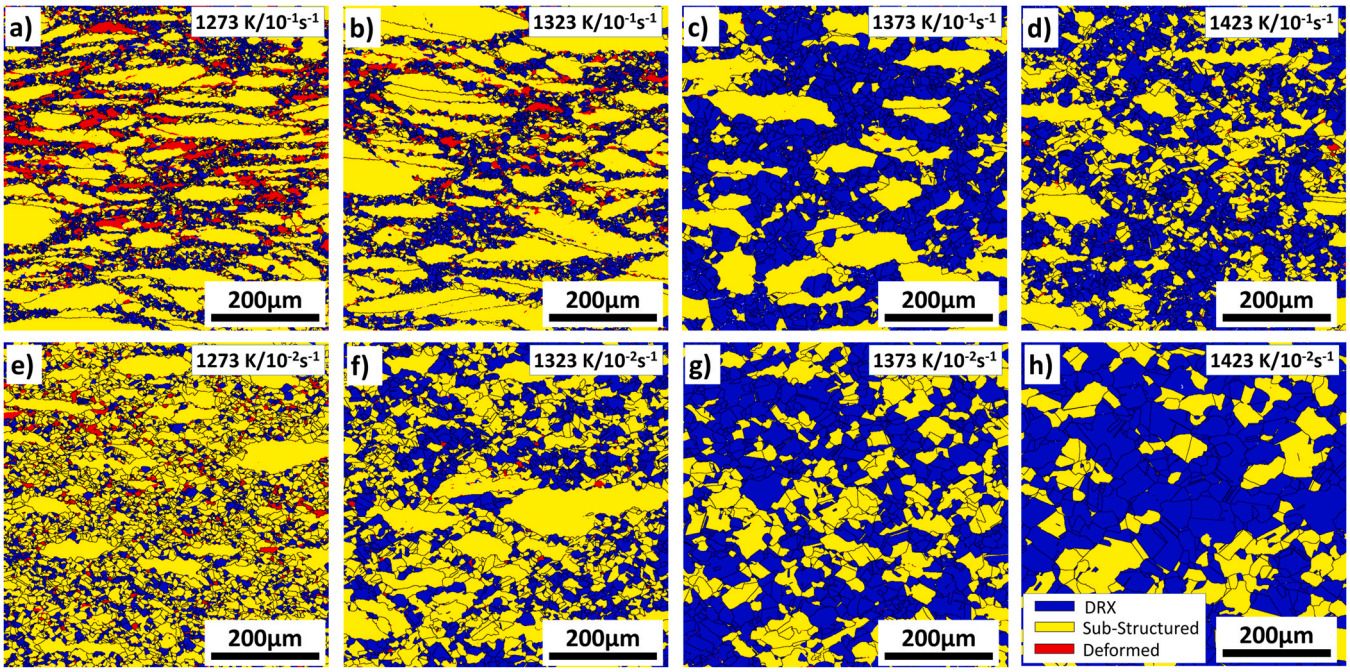

Fig. 10. GAM maps of $Al_{0.3}$CoCrFeNi HEA deformed at (a)1273 K/10^{-1} s^{-1}; (b) 1323 K/$10^{-1}s^{-1}$; (c)1373 K/$10^{-1}s^{-1}$; (d) 1423 K/10^{-1} s^{-1}; (e)1273 K/10^{-2} s^{-1}; (f) 1323 K/10^{-2} s^{-1}; (g) 1373 K/10^{-2} s^{-1}; (h) 1423 K/10^{-2} s^{-1}.

process less efficient in respect of power dissipation because of the hindrance to the dislocation motion by the dynamically precipitated B_2 particles.

3.4.4. Region E (Low efficiency regime at 1423 K/10^{-3} s^{-1})

This regime occurs in the bottom right corner of the processing map, in the temperature range of 1323–1423 K and a narrow strain rate range of 5×10^{-3}–10^{-3} s^{-1}. This regime showed a sharp decrease in η value with closely spaced iso–efficiency contours. The η value at 1423 K/10^{-3} s^{-1} was recorded as 21.4% at 0.2ε, dropping further to 11.7% at 0.7ε. The micrographs at 1373 K/10^{-3} s^{-1} and 1423 K/10^{-3} s^{-1} clearly revealed nucleation of wedge cracks along the GB triple point junction, etc., as marked by arrows in Fig. 14a and b. In this condition, there is a possibility of extensive grain growth due to annealing at high temperatures. However, this regime is not desirable for hot working due to the sharp decrease in η value, the formation of wedge cracks along the triple–point junctions of the GBs and grain coarsening.

3.4.5. Region A (instability manifestation)

The flow instability is expected to manifest in the microstructure, whenever the instability parameter $\xi(\dot{\varepsilon})$ value turns negative. The regions marked with red color in the processing map (Fig. 6c) correspond to the instability regime, as demarcated by negative values of $\xi(\dot{\varepsilon})$ in the instability map constructed for a true strain of 0.6, Fig. S3d. Deformation within this regime may exhibit the manifestation of various microstructural defects, such as GB cracks, adiabatic shear bands and flow localization [40]. In order to validate the regime, a detailed microstructural evaluation was performed for the selected specimens corresponding to the instability regime. It is observed that the increase in strain rate increased the temperature range of the instability regime. At strain rates $\geq 3 \times 10^{-1}$ s^{-1}, the instability regime covered the entire temperature range, Fig. 6a–c. This is because the time available for the dislocation motion to avoid the defects decreases with the increase in strain rate.

The instability region at 10^{-2} s^{-1} extends to a short temperature range of 1023–1073 K. At low strain rates between 10^{-2}–10^{-1} s^{-1}, the flow curves (Fig. 2a–c) showed mild softening behavior that decreased with an increase in the strain rate. A representative optical micrograph of this region corresponding to the specimen deformed at 1023 K/10^{-2} s^{-1} is shown in Fig. 15a, revealing intense cracks along the grain boundaries. The GB cracks or sliding can occur at low strain rates and temperatures, as the slower dislocation motion render the distribution of the dislocations non–uniform, thereby causing dislocation pile–up along the GBs and facilitating GB cracks. [14]. With the increase in temperature, the GB cracking tendency decreases with enhanced dislocation passage. Patnamsetty et al. [29] reported the hot deformation behavior of an FCC CoCrFeMnNi HEA, where the tendency of GB cracking was clearly revealed for a regime extending over strain rate and temperature ranges of 10^{-3}–10^{-2} s^{-1} and temperatures range 1023–1123 K, with the tendency of GB cracking decreasing with the increase in temperature.

Further increase in strain rate to 3×10^{-1} s^{-1} extended the instability regime over the entire temperature range from 1023 to 1423 K. The flow stress curves at 1023–1123 K at the strain rates of 1 and 10 s^{-1} (Fig. 2a–e) have shown work hardening behavior, which resulted in generation of high dislocation density. At low temperatures, i.e., ≤ 1223 K and at strain rates > 3×10^{-1} s^{-1}, work hardening resulted in the microstructural changes such as dislocation glide and grain distortion, in addition to the occurrence of the visco–plastic heat. If the respective visco–plastic heat generated doesn't have sufficient time to escape or dissipate, the localized deformation due to the heating can lead to the formation of the adiabatic shear bands [14]. Fig. 15b and c confirm the existence of adiabatic shear bands and distorted grains in samples deformed at 1023 K/1 s^{-1} and 1223 K/1 s^{-1}, respectively. A similar behavior of instabilities was previously observed in the case of CoCrFeMnNi deformed at 1023–1223 K/1–10 s^{-1} [29]. The effect of adiabatic shear band formation and grain distortion decreased with an increase in temperature and a decrease in strain rate. The presence of shear bands/

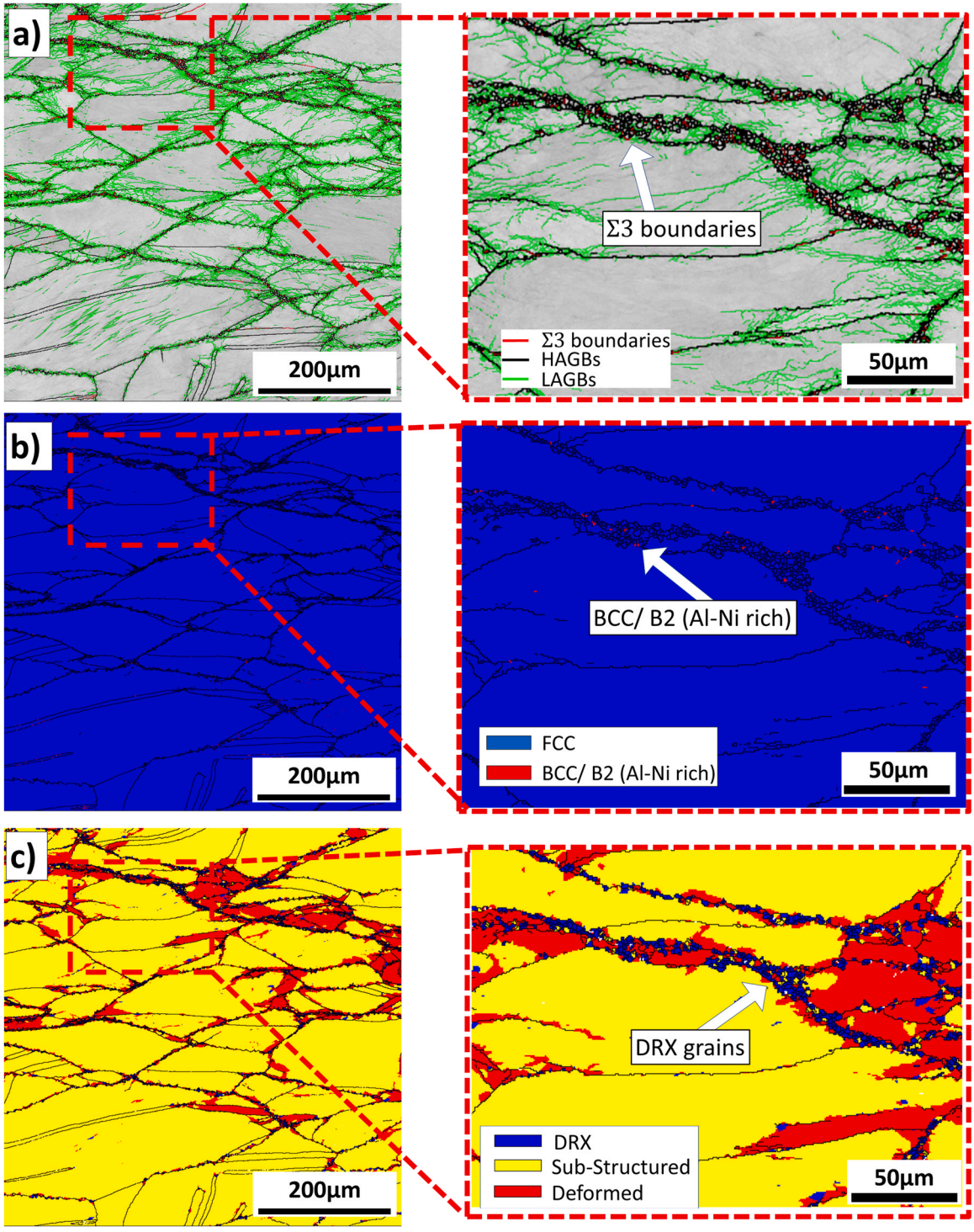

Fig. 11. a) IQ map, b) Phase fraction map & c) GAM map of $Al_{0.3}CoCrFeNi$ alloy hot deformed at 1123 K/10^{-3} s^{-1} (Insets of the specific cross section included with higher magnification).

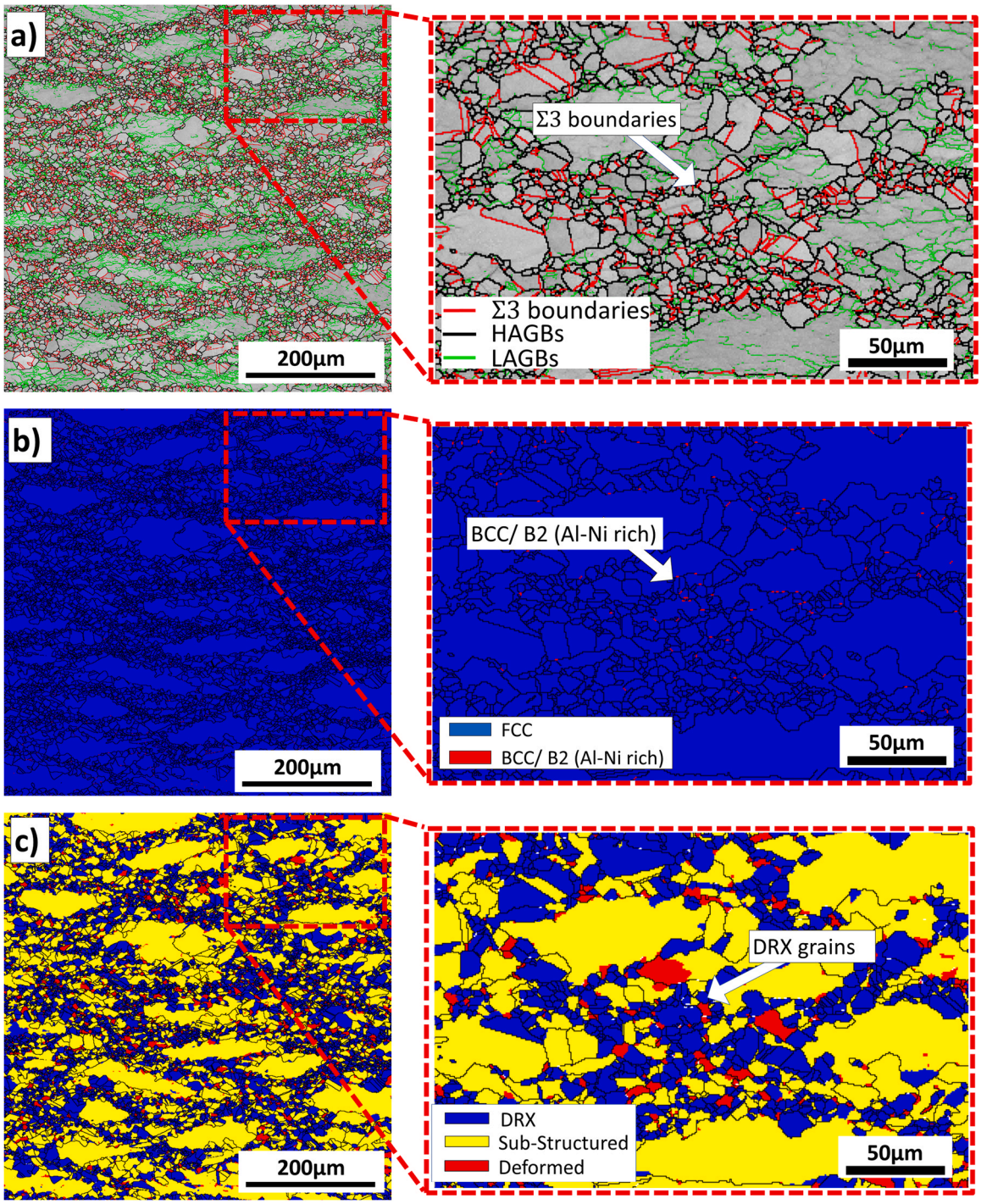

Fig. 12. a) IQ map, b) Phase fraction map & c) GAM map of $Al_{0.3}CoCrFeNi$ HEA hot deformed at 1223 K/10^{-3} s^{-1}.

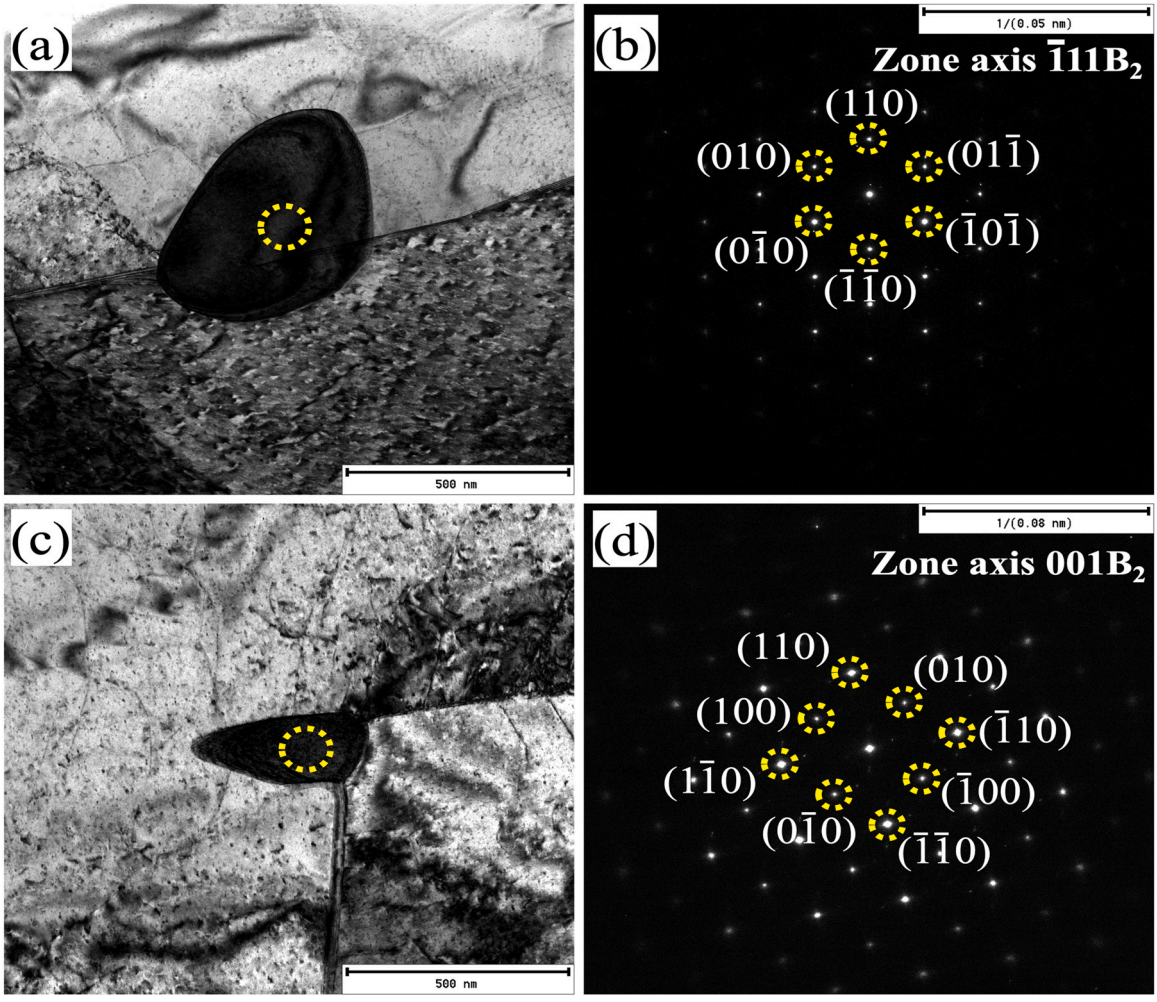

Fig. 13. TEM bright field image of the precipitates (a, c) and the corresponding SAED patterns (b, d).

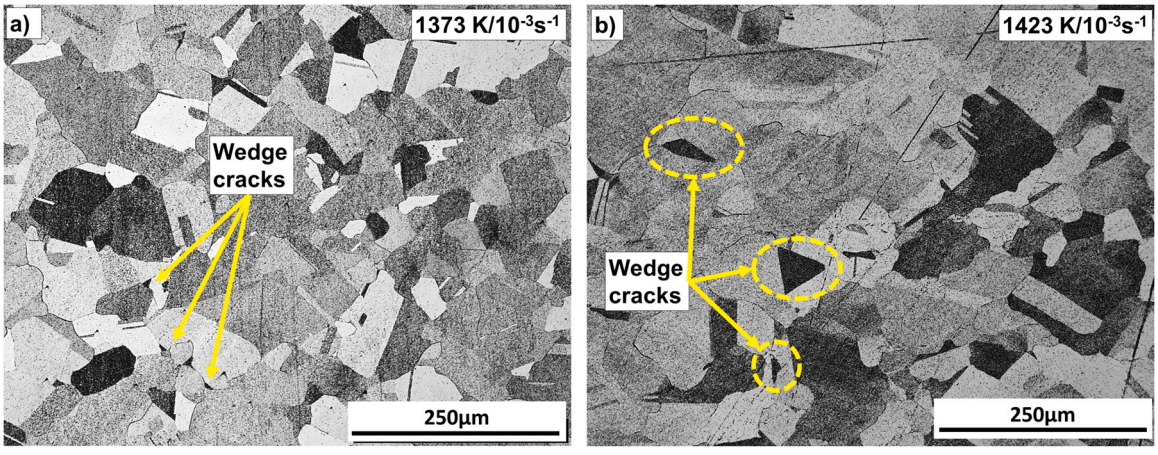

Fig. 14. Optical micrograph of $Al_{0.3}$CoCrFeNi HEA hot deformed at (a) 1373 K/10^{-3} s^{-1}, (b) 1423 K/10^{-3} s^{-1}.

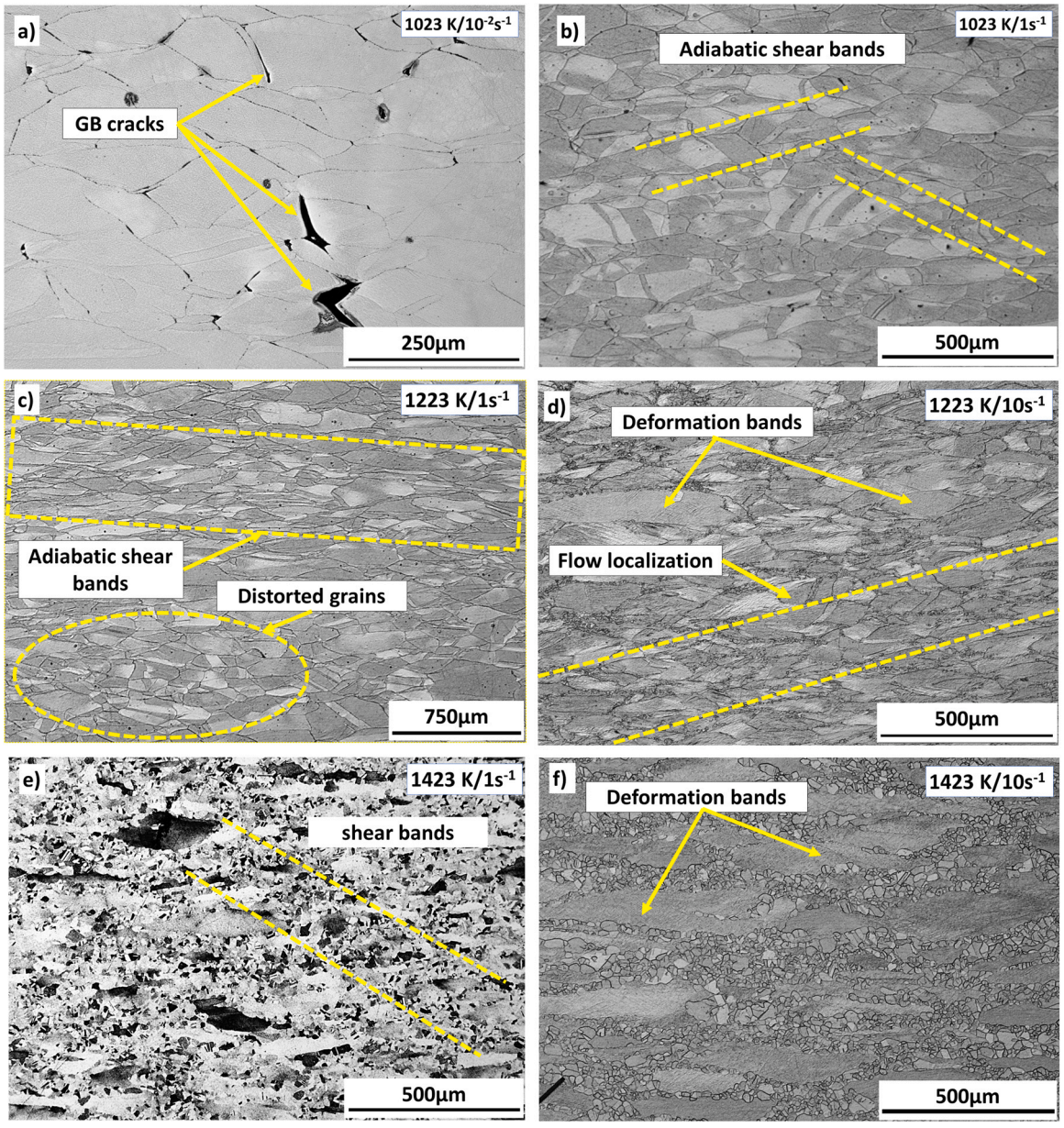

Fig. 15. Optical micrograph of $Al_{0.3}CoCrFeNi$ HEA hot deformed (a) 1023 K/10^{-2} s^{-1}; (b) 1023 K/1 s^{-1}; (c)1223 K/1 s^{-1}; (d) 1423 K/1 s^{-1}; (e) 1223 K/10 s^{-1}; (f) 1423 K/10 s^{-1}.

flow localization and highly deformed grains is clearly seen in Fig. 15d, which shows the decrease in the effect of grain distortion with most of the grains in highly deformed condition. Therefore, the hot deformation behavior changes from work hardening to other mechanisms with an increase in temperature, such as the occurrence of DRX in the adiabatic shear bands at intermediate and high strain rates in the case of low SFE materials.

At higher temperatures > 1223 K, the flow stress curves showed softening behavior at 1 s^{-1} after a peak stress around 0.4 – 0.5 ε, Fig. 3(f)–(i). It is observed that the deformation mechanism changed with an increase in temperature from work hardening to the formation of recrystallized grains along the instabilities, such as shear bands and/or localized deformation in grains. The specimen deformed at 1423 K/1 s^{-1} exhibited a small fraction of DRX gains formed along the shear bands (Fig. 15e). In addition, the occurrence of some texture is apparent, suggesting a preferred orientation of the elongated grains and random orientation of the DRX grains. Finally, at high temperatures (> 1223 K) and at the highest strain rate in our case (10 s^{-1}), the flow stress curves showed a steady-state behavior, Fig. 3f – i. The representative micrograph at 1423 K/10 s^{-1} (Fig. 15f) showed fine DRX grains occurring along the GBs oriented along the deformation bands. Therefore, as explained above this regime is not safe for hot working, due to the manifestation of instabilities.

3.4.6. Summary of hot deformation mechanisms

Based on the outcome of dynamic material modelling and constitutive flow behavior supported by the microstructural characterization, a conceptual processing map (Fig. 7a) was proposed, for hot working of $Al_{0.3}CoCrFeNi$ in the temperature range of 1023–1423 K and strain rate range of 10^{-3}–10 s^{-1}. The DRX domain extending over the temperature range of 1273–1423 K and strain rate range of 2×10^{-2}–10^{-3} s^{-1}, is identified as a 'safe' workable domain for the alloy. Furthermore, the DRV domain at 1123 K/10^{-3} s^{-1} and the low efficiency regime at 1223 K/10^{-3} s^{-1} showed the formation of B_2 precipitates that act as nucleation sites for DRX grains via PSN mechanism. However, the precipitation of B_2 phase is sluggish in the DRV domain, and the dominant microstructural mechanism still remains to be dynamic recovery. Table 3 lists the values of

Table 3
Summary of hot deformation mechanisms of hot rolled $Al_{0.3}CoCrFeNi$ at $\varepsilon = 0.6$.

Region	T range (K)	$\dot{\varepsilon}$ range (s^{-1})	η range (value) %	ξ range (value)	Key microstructural features	Broad mechanisms
A	1023–1423 (Instability regime)	10^{-2}–10	2–40	−0.79 to 0.37	Localized shear bands, adiabatic shear bands, GB cracking/sliding	Manifestation of instabilities
B	1273–1423 (Deterministic domain)	2×10^{-1}–10^{-2}	36–45	0.1–0.48	Recrystallization and grain growth	DRX
C	1073–1148	3×10^{-3}–10^{-3}	31–37	0.06–0.52	DRV, trace DRX or SRX grains via PSN	DRV
D	1148–1298	5×10^{-3}–10^{-3}	32–8	0.25–0.65	Dynamic precipitation with PSN of DRX grains	Dynamic precipitation; partial DRX via PSN
E	1323–1423	5×10^{-3}–10^{-3}	11–40	0.15–0.64	Wedge cracks, grain coarsening	Cavitation/cracks at grain boundaries

dimensionless parameters (η and ξ) of different domains / regimes along with their operating microstructural mechanisms.

4. Conclusions

This study encompasses the evaluation of constitutive flow behavior, dynamic microstructural evolution, and hot workability of a hot rolled $Al_{0.3}CoCrFeNi$ based on the experimental true stress–true strain data obtained via isothermal hot compression testing on a Gleeble simulator, over the broad temperature ranges of 1023–1423 K and strain rate range of 10^{-3}–10 s^{-1}, respectively, deformed to a true strain of ~0.75. A hyperbolic–sinusoidal Arrhenius–type constitutive equation was developed to describe the constitutive flow stress behavior over a true strain range of 0.2 – 0.75. In order to assess the intrinsic workability of the alloy, the DMM principles were used to construct a processing map, characterize the dynamic materials behavior, and identify a 'safe' processing window suitable for the deformation processing of the alloy. The following conclusions can be drawn from this work:

1) The flow curves showed peak stress behavior at lower strain rates (10^{-3}–10^{-1} s^{-1}), followed by flow softening. In addition, at temperatures ≤ 1123 K and strain rates > 1 s^{-1}, the flow stress values increased with an increase in strain, apparently due to enhanced strain hardening as a result of continued deformation. Further increase in temperature at high strain rates resulted in flow stress behavior becoming nearly steady – state with increased straining.
2) An Arrhenius type hyperbolic–sinusoidal constitutive equation was established for high temperature deformation in the true strain range of 0.2 – 0.75 and the equation is valid for the temperature and strain rate ranges of 1023–1423 K and 10^{-3}–10 s^{-1} respectively. The activation energy of deformation (Q_{def}) and material constants (A, α and n) were determined and linked with their dependence on strain. Polynomial equations (6th order) were developed by the regression analysis of the flow stress data to express the material constants as a function of strain for this alloy.
3) The Q_{def} at $\varepsilon = 0.6$ was calculated to be ~308 kJ with the stress component $n = 4.318$. This Q_{def} value decreases from ~410 to ~302 kJ/mol with an increase in true strain (ε) value from 0.2 to 0.75. A comparison of the experimental and predicted flow stress data suggests AARE and correlation coefficient R of 9.66% and 0.9781, respectively, thus confirming the suitability of constitutive equations in predicting the flow stress over a broad temperature, strain rate, and strain conditions.
4) A processing map was developed using the principles of DMM, thereby identifying various domains, and low efficiency and instability regimes typical of various microstructural mechanisms occurring during hot deformation under the respective conditions. The domain extending over 1273–1423 K/10^{-2}–2×10^{-2} s^{-1} was identified as the 'safe' workable domain comprising DRX as the operating microstructural mechanism.
5) A DRV domain was identified extending over 1048–1148 K/ 10^{-3}–3×10^{-3} s^{-1}. The presence of traces of fine grains along the boundaries has been correlated to the formation of B_2 precipitates that triggered PSN of dynamically or even statically recrystallized grains. However, the dominant microstructural mechanism in this domain is DRV.
6) The deformation in the temperatures range of 1148–1298 K at low strain rates in the narrow range of 5×10^{-3}–10^{-3} s^{-1} led to the dynamic precipitation of B_2 precipitates, which resulted in PSN of DRX grains, though η was low (9%) and continued to drop towards the center of the regime (1223 K/10^{-3} s^{-1}). Tentatively, it seems that the interaction of DRX grain boundaries with precipitates resulted in a reduction of the dissipation of power through microstructural mechanisms, thus lowering ~ η.

7) The entire deformation space above 3×10^{-1} s^{-1} practically falls in the instability regime, which is not suitable for hot working. At lower strain rates between 10^{-2}–10^{-1} s^{-1}, the deformation region below 1123 K also falls under the instability regime. This regime is prone to various microstructural defects such as adiabatic shear bands, flow localization and GB sliding/cracking, etc. In addition, a small cracking regime was identified in the high temperature and low strain rate region extending over 1323–1423 K and 5×10^{-3}–10^{-3} s^{-1}, respectively. The regime with closely spaced iso–efficiency contours has shown a sharp decrease in the efficiency of power dissipation (12%) and the microstructural mechanism in this region was identified as the formation of wedge cracking/cavitation, particularly at triple–-point junctions of the GBs.

CRediT authorship contribution statement

Madan Patnamsetty: Conceptualization, Methodology, Investigation, Software, Writing – original draft. **Sumit Ghosh:** Methodology, Investigation, Writing – review & editing. **Mahesh C. Somani:** Conceptualization, Methodology, Supervision, Validation, Writing – review & editing. **Pasi Peura:** Validation, Supervision, Resources, Funding acquisition.

Data Availability

Original data will be made available by the authors on request.

Declaration of Competing Interest

The authors declare that they have no known competing financial interests or personal relationships that could have appeared to influence the work reported in this paper.

Acknowledgements

Authors acknowledge Tampere University Foundation as a part of Tampere University's Graduate School, and Walter Ahlström Foundation and Ella Georg Ehrnrooth Foundation for the financial support. In addition, this work made use of Tampere Microscopy Centre facilities at Tampere University and transmission electron microscopy facilities at Centre for Material Analysis, University of Oulu. The authors would also like to thank Mr. Jussi Paavola for laboratory rolling, Mr. Juha Uusitalo for performing the Gleeble simulation experiments, and Mr. Sami Saukko for conducting the TEM investigation.

Appendix A. Supporting information

Supplementary data associated with this article can be found in the online version at doi:10.1016/j.jallcom.2022.165341.

References

[1] E.P. George, D. Raabe, R.O. Ritchie, High-entropy alloys, Nat. Rev. Mater. 4 (2019) 515–534, https://doi.org/10.1038/s41578-019-0121-4
[2] B. Cantor, I.T.H. Chang, P. Knight, A.J.B. Vincent, Microstructural development in equiatomic multicomponent alloys, Mater. Sci. Eng. A 375–377 (2004) 213–218, https://doi.org/10.1016/j.msea.2003.10.257
[3] E.P. George, W.A. Curtin, C.C. Tasan, High entropy alloys: a focused review of mechanical properties and deformation mechanisms, Acta Mater. 188 (2020) 435–474, https://doi.org/10.1016/j.actamat.2019.12.015
[4] Z. Li, A. Ludwig, A. Savan, H. Springer, D. Raabe, Combinatorial metallurgical synthesis and processing of high-entropy alloys, J. Mater. Res. 33 (2018) 3156–3169, https://doi.org/10.1557/jmr.2018.214
[5] W.-R. Wang, W.-L. Wang, S.-C. Wang, Y.-C. Tsai, C.-H. Lai, J.-W. Yeh, Effects of Al addition on the microstructure and mechanical property of AlxCoCrFeNi high-entropy alloys, Intermetallics 26 (2012) 44–51, https://doi.org/10.1016/j.intermet.2012.03.005
[6] Y.-F. Kao, T.-J. Chen, S.-K. Chen, J.-W. Yeh, Microstructure and mechanical property of as-cast, -homogenized, and -deformed AlxCoCrFeNi (0≤x≤2) high-entropy alloys, J. Alloy. Compd. 488 (2009) 57–64, https://doi.org/10.1016/j.jallcom.2009.08.090
[7] J. Li, H. Yang, W.Y. Wang, H. Kou, J. Wang, Thermal–mechanical processing and strengthen in AlxCoCrFeNi high-entropy alloys, Front. Mater. 7 (2021), https://doi.org/10.3389/fmats.2020.585602
[8] B. Gwalani, V. Soni, M. Lee, S. Mantri, Y. Ren, R. Banerjee, Optimizing the coupled effects of Hall-Petch and precipitation strengthening in a Al 0.3 CoCrFeNi high entropy alloy, Mater. Des. 121 (2017) 254–260, https://doi.org/10.1016/j.matdes.2017.02.072
[9] X. Wang, Z. Zhang, Z. Wang, X. Ren, Microstructural evolution and tensile properties of Al0.3CoCrFeNi high-entropy alloy associated with B2 precipitates, Materials 15 (2022) 1215, https://doi.org/10.3390/ma15031215
[10] S. Muskeri, B. Gwalani, S. Jha, A. Yu, P.A. Jannotti, R.S. Haridas, B.E. Schuster, J.T. Lloyd, R.S. Mishra, S. Mukherjee, Excellent ballistic impact resistance of Al0.3CoCrFeNi multi-principal element alloy with unique bimodal microstructure, Sci. Rep. 11 (2021) 22715, https://doi.org/10.1038/s41598-021-02209-y
[11] S. Xie, J. Zhang, R. Li, T. Yuan, M. Zhang, M. Wang, Z. Zhang, S. Deng, Q. Li, Accelerated precipitation of the B2 particles and its effect on Al0.3CoCrFeNi high-entropy alloy by electric current assisted annealing, Mater. Charact. 181 (2021) 111434, https://doi.org/10.1016/j.matchar.2021.111434
[12] K. Liu, M. Komarasamy, B. Gwalani, S. Shukla, R.S. Mishra, Fatigue behavior of ultrafine grained triplex Al0.3CoCrFeNi high entropy alloy, Scr. Mater. 158 (2019) 116–120, https://doi.org/10.1016/j.scriptamat.2018.08.048
[13] S. Dasari, A. Sarkar, A. Sharma, B. Gwalani, D. Choudhuri, V. Soni, S. Manda, I. Samajdar, R. Banerjee, Recovery of cold-worked Al0.3CoCrFeNi complex concentrated alloy through twinning assisted B2 precipitation, Acta Mater. 202 (2021) 448–462, https://doi.org/10.1016/J.ACTAMAT.2020.10.071
[14] Y.V.R.K. Prasad, K.P. Rao, S. Sasidhara, Hot Working Guide: A Compendium of Processing Maps, Second Edition - Google Books, ASM International, 2015.
[15] N. Haghdadi, S. Primig, M. Annasamy, P. Cizek, P.D. Hodgson, D.M. Fabijanic, On the hot-worked microstructure of a face-centered cubic Al0.3CoCrFeNi high entropy alloy, Scr. Mater. 178 (2020) 144–149, https://doi.org/10.1016/j.scriptamat.2019.11.022
[16] Y. Tong, J.C. Qiao, Y. Yao, The constitutive model and threshold stress for characterizing the deformation mechanism of Al0.3CoCrFeNi high entropy alloy, Mater. Sci. Eng. A 730 (2018) 137–146, https://doi.org/10.1016/j.msea.2018.05.109
[17] Y. Zhang, J. Li, J. Wang, S. Niu, H. Kou, Hot deformation behavior of As-cast and homogenized Al0.5CoCrFeNi high entropy alloys, Metals 6 (2016) 277, https://doi.org/10.3390/met6110277
[18] H.T. Jeong, H.K. Park, W.J. Kim, Dynamic recrystallization and hot deformation mechanisms of a eutectic Al0.7CoCrFeMnNi high-entropy alloy, J. Alloy. Compd. 871 (2021) 159488, https://doi.org/10.1016/J.JALLCOM.2021.159488
[19] J. Wang, H. Li, H. Yang, Y. Zhang, W.Y. Wang, J. Li, Hot deformation and subsequent annealing on the microstructure and hardness of an Al0.3CoCrFeNi high-entropy alloy, Acta Metall. Sin. (Engl. Lett.) 34 (2021) 1527–1536, https://doi.org/10.1007/s40195-021-01251-z
[20] B. Gwalani, R. Salloom, T. Alam, S.G. Valentin, X. Zhou, G. Thompson, S.G. Srinivasan, R. Banerjee, Composition-dependent apparent activation-energy and sluggish grain-growth in high entropy alloys, Mater. Res. Lett. 7 (2019) 267–274, https://doi.org/10.1080/21663831.2019.1601644
[21] M. Annasamy, N. Haghdadi, A. Taylor, P. Hodgson, D. Fabijanic, Static recrystallization and grain growth behaviour of Al0.3CoCrFeNi high entropy alloy, Mater. Sci. Eng. A 754 (2019) 282–294, https://doi.org/10.1016/j.msea.2019.03.088
[22] F.J. Zerilli, R.W. Armstrong, Dislocation-mechanics-based constitutive relations for material dynamics calculations, J. Appl. Phys. 61 (1987) 1816–1825, https://doi.org/10.1063/1.338024
[23] G. Mahalle, O. Salunke, N. Kotkunde, A. Kumar Gupta, S.K. Singh, Study of Khan-Huang-Liang (KHL) anisotropic deformation model for deep drawing behaviour of Inconel 718 Alloy, IOP Conf. Ser. Mater. Sci. Eng. 967 (2020) 012054, https://doi.org/10.1088/1757-899X/967/1/012054
[24] G.R. Johnson, W.H. Cook, Fracture characteristics of three metals subjected to various strains, strain rates, temperatures and pressures, Eng. Fract. Mech. 21 (1985) 31–48, https://doi.org/10.1016/0013-7944(85)90052-9
[25] C.M. Sellars, W.J. McTegart, On the mechanism of hot deformation, Acta Met. 14 (1966) 1136–1138, https://doi.org/10.1016/0001-6160(66)90207-0
[26] Z. Savaedi, R. Motallebi, H. Mirzadeh, A review of hot deformation behavior and constitutive models to predict flow stress of high-entropy alloys, J. Alloy. Compd. 903 (2022) 163964, https://doi.org/10.1016/J.JALLCOM.2022.163964
[27] M. Patnamsetty, A. Saastamoinen, M.C. Somani, P. Peura, Constitutive modelling of hot deformation behaviour of a CoCrFeMnNi high-entropy alloy, Sci. Technol. Adv. Mater. 21 (2020) 43–55, https://doi.org/10.1080/14686996.2020.1714476
[28] S.A. Sajadi, M.R. Toroghinejad, A. Rezaeian, G.R. Ebrahimi, A study of hot compression behavior of an as-cast FeCrCuNi2Mn2 high-entropy alloy, J. Alloy. Compd. 896 (2022) 162732, https://doi.org/10.1016/j.jallcom.2021.162732
[29] M. Patnamsetty, M.C. Somani, S. Ghosh, S. Ahmed, P. Peura, Processing map for controlling microstructure and unraveling various deformation mechanisms during hot working of CoCrFeMnNi high entropy alloy, Mater. Sci. Eng. A 793 (2020) 139840, https://doi.org/10.1016/j.msea.2020.139840
[30] W.J. Kim, H.T. Jeong, H.K. Park, K. Park, T.W. Na, E. Choi, The effect of Al to high-temperature deformation mechanisms and processing maps of Al0.5CoCrFeMnNi high entropy alloy, J. Alloy. Compd. 802 (2019) 152–165, https://doi.org/10.1016/j.jallcom.2019.06.099

[31] H.T. Jeong, H.K. Park, W.J. Kim, Hot deformation behavior and processing map of a Sn0.5CoCrFeMnNi high entropy alloy with dual phases, Mater. Sci. Eng. A 801 (2021) 140394, https://doi.org/10.1016/j.msea.2020.140394
[32] F. Dong, Y. Yuan, W. Li, Y. Zhang, P.K. Liaw, X. Yuan, H. Huang, Hot deformation behavior and processing maps of an equiatomic MoNbHfZrTi refractory high entropy alloy, Intermetallics 126 (2020) 106921, https://doi.org/10.1016/j.intermet.2020.106921
[33] S. Ghosh, M. Patnamsetty, M.C. Somani, P. Peura, Characteristics of dynamic softening during high temperature deformation of CoCrFeMnNi high-entropy alloy and its correlation with the evolving microstructure and micro-texture, J. Mater. Res. Technol. 15 (2021) 6608–6623, https://doi.org/10.1016/j.jmrt.2021.11.089
[34] G. Ge, L. Zhang, J. Xin, J. Lin, M. Aindow, L. Zhang, Constitutive modeling of high temperature flow behavior in a Ti-45Al-8Nb-2Cr-2Mn-0.2Y alloy, Sci. Rep. 8 (2018) 5453, https://doi.org/10.1038/s41598-018-23617-7
[35] Z. Li, F. Körmann, B. Grabowski, J. Neugebauer, D. Raabe, Ab initio assisted design of quinary dual-phase high-entropy alloys with transformation-induced plasticity, Acta Mater. 136 (2017) 262–270, https://doi.org/10.1016/j.actamat.2017.07.023
[36] F. He, Z. Wang, B. Han, Q. Wu, D. Chen, J. Li, J. Wang, C.T. Liu, J.J. Kai, Solid solubility, precipitates, and stacking fault energy of micro-alloyed CoCrFeNi high entropy alloys, J. Alloy. Compd. 769 (2018) 490–502, https://doi.org/10.1016/J.JALLCOM.2018.07.336
[37] Z. Li, S. Zhao, H. Diao, P.K. Liaw, M.A. Meyers, High-velocity deformation of Al0.3CoCrFeNi high-entropy alloy: remarkable resistance to shear failure, Sci. Rep. 7 (2017) 42742, https://doi.org/10.1038/srep42742
[38] K. Huang, R.E. Logé, A review of dynamic recrystallization phenomena in metallic materials, Mater. Des. 111 (2016) 548–574, https://doi.org/10.1016/j.matdes.2016.09.012
[39] F.J. Humphreys, M. Hatherly, Recovery and recrystallization during and after hot deformation, Recryst. Relat. Annealing Phenom. (1995) 363–392, https://doi.org/10.1016/B978-0-08-041884-1.50018-0
[40] M.C. Somani, K. Muraleedharan, Y.V.R.K. Prasad, V. Singh, Mechanical processing and microstructural control in hot working of hot isostatically pressed P/M IN-100 superalloy, Mater. Sci. Eng. A 245 (1998) 88–99, https://doi.org/10.1016/S0921-5093(97)00698-9